2018

Pyrolysis of Fiber-Plastic Waste Blends

Shreyas Kolapkar
Michigan Technological University, sskolapk@mtu.edu

PYROLYSIS OF FIBER-PLASTIC WASTE BLENDS

By

Shreyas S. Kolapkar

A THESIS

Submitted in partial fulfillment of the requirements for the degree of

MASTER OF SCIENCE

In Mechanical Engineering

MICHIGAN TECHNOLOGICAL UNIVERSITY

2018

This thesis has been approved in partial fulfillment of the requirements for the Degree of MASTER OF SCIENCE in Mechanical Engineering.

Department of Mechanical Engineering - Engineering Mechanics

Thesis Advisor:	*Dr. Ezra Bar-Ziv*
Committee Member:	*Dr. David Shonnard*
Committee Member:	*Dr. Jeffrey Naber*
Committee Member:	*Dr. Jordan Klinger*

Department Chair: Dr. William Predebon

Table of Contents

List of figures v
Preface vii
Acknowledgments ix
Abstract x
1 Introduction 1
1.1 Motivation 1
1.2 Background 3
1.3 Literature review 5
1.4 The paddle reactor 10
2 Research objective 13
3 Materials and methods 15
3.1 Feedstock material 15
3.2 Methods 18
3.2.1 Batch pyrolysis 18
3.2.2 Continuous paddle reactor pyrolysis 20
3.2.3 Chlorine removal 24
4 Characterization 27
4.1 Proximate analysis 27
4.2 Ultimate analysis 27
4.3 Gas chromatography - mass spectrometry (GC-MS) 28
4.4 Electro-spray ionization - mass spectrometry (ESI-MS) 30
4.5 Fourier transform infrared spectrometry (FTIR) 31
4.6 Photometry for chloride measurement 32
5 Current results 34
5.1 Feedstock characterization 34
5.2 Heat transfer analysis 36
5.2.1 Batch 36
5.2.2 Continuous paddle 40

5.3 Pyrolysis oil....42
5.4 Pyrolysis-oil characterization....43
5.4.1 Fiber....43
5.4.1.1 FTIR....44
5.4.1.2 HPLC....45
5.4.1.3 GC-MS....46
5.4.1.4 ESI-MS....47
5.4.2 Plastic....49
5.4.2.1 GC-MS....49
5.4.2.2 Chlorine removal....50
5.4.3 Fiber-plastic blend....51
5.4.3.1 FTIR....51
5.4.3.2 Chlorine content....52
6 Future work....54
7 Reference List....61
Appendix....68

List of figures

Figure 1: CE feedstocks (A) fiber/paper (B) plastic (C) loose fiber-plastic waste-blends (D) densified fiber-plastic blend pellets.....15

Figure 2: Feedstock characterization on quarterly basis from year 2011 to 2017 by CE.....17

Figure 3: Batch pyrolysis schematic.....18

Figure 4: Paddle reactor schematic.....20

Figure 5: Cartoon of paddle reactor system.....21

Figure 6: Left - Temperature profiles for heater 1, 4, 5 and 10 in 1-inch system. Right - Temperature distribution vs. axial co-ordinate for 1-inch pyrolysis system.....22

Figure 7: Solid-works model showing the design of 4-inch continuous paddle reactor system.....24

Figure 8: (A) The 4-inch reactor showing band heaters and thermocouple connections (B) Reactor paddle shaft.....24

Figure 9: (A) Charles Ross & Son Company's (Model HSM-100-LSK-1) high shear mixer used in chlorine removal. (B) Chlorine filtration setup.....26

Figure 10: Gas Chromatography-Mass Spectrometry (GC-MS) block diagram.....29

Figure 11: ESI-MS block diagram.....30

Figure 12: Fourier transform infrared spectrometry block diagram (FTIR).....31

Figure 13: Photometer used for Chloride measurement.....33

Figure 14: Ash content distribution.....35

Figure 15 Temperature transients for batch reactor (fiber/plastic material) based on model with characteristic time of ~28 (s).....40

Figure 16: State of particles at various paddle speeds (suspension).....41

Figure 17: Temperature vs. time plot for continuous paddle reactor based on model. ...42

Figure 18: Top fraction (left) and bottom fraction (right) of pyrolysis oil from fiber. ...44

Figure 19: FTIR spectra of pyrolysis bio-oil top and bottom layers.....45

Figure 20: GC-MS analysis of fiber/paper pyrolysis oil from bottom layer.....46

Figure 21: Negative ion ESI-MS of bio-oil top layer (cellulose) and bottom layer (lignin) showing mass spectrum (Top) in m/z= 100 to m/z=1500 range. (Bottom) overlap in m/z= 100 to m/z=250 range. 47
Figure 22: Cumulative mass (m/z) from range of 100 to 300 showing inversion of lignin and cellulose production trend after m/z of 180. 48
Figure 23: GC-MS (TIC) of bio-oil from plastic feedstock. 49
Figure 24: GC-MS (TIC) of diesel sample. 50
Figure 25: Comparison of GC-MS of plastic oil and diesel. 50
Figure 26: (Left) Mass loss for plastic (Right) Chlorine removal vs. high shear mixing time. 51
Figure 27: FTIR spectra of CE-fiber mix and ground/screened (425-850 μm) torrefied (10, 20 and 42% mass loss) densified material. 52
Figure 28: (left) Mass loss vs. time (right) chloride in solid filtrate after high shear and chlorine in aqueous solution. 53
Figure 29: Effect of heating rate in P instantaneous vs time plot. 57

List of tables

Table 1: Typical parameters and product yields for different types of pyrolysis 4
Table 2: Feedstock physical attributes and their effects on pyrolysis 27
Table 3: Feedstock chemical attributes and their effects on pyrolysis process and product. 28
Table 4: Proximate analysis of CE waste-blend feedstock 34
Table 5: Characterization of ash 34
Table 6: Ultimate analysis of feedstock 35
Table 7: Other elements found in the feedstock. 35
Table 8: Estimated values for the parameters to determine the Bi and M. 38
Table 9: Pyrolysis oil from fiber feedstock 43
Table 10: Compounds from cellulose. 45

Preface

The current report contains results for my master's thesis in partial fulfillments of the requirements for the degree of MASTER OF SCIENCE in Mechanical Engineering. The report also contains results, ideas, and future work for a Ph.D. thesis. Thus, the report should be perceived as both my master's thesis as well as my Ph.D. thesis proposal.

Chapter 1, Chapter 3 (3.1, 3.2.1 and part of 3.2.3), Chapter 4, Chapter 5 (5.1, 5.2.1, 5.3, 5.4) and conclusions in Chapter 6 are part of the master's thesis work. The remaining complimentary chapters: Chapter 2, Chapter 3 (3.2.3) and future work in Chapter 6 are part of continued doctoral work. Furthermore, Chapter 5 shows current results for master's thesis work which will be further expanded in the doctoral work.

Further, the author of this thesis has one published paper (attached here) and another paper is currently under preparation. The full citation details of the published work are follows:

Z. Xu, S. Zinchik, S.S. Kolapkar, E. Bar-Ziv, T. Hansen, D. Conn, A.G. McDonald, Properties of Torrefied U.S. Waste Blends, Front. Energy Res. 6 (2018) 1–13. doi:10.3389/fenrg.2018.00065.

Author contributions:

SK worked in a team where each member contributed in part to the entire work, however, each member was responsible for a specific part of work that is related to their own thesis work. SK is responsible for the pyrolysis work and has been focusing on its aspects.

The following help was obtained by the various member from the team: ZX conducted torrefaction experiments and characterization for heat and moisture content, grinding and size fractions. Torrefaction was used in this thesis for chlorine removal. SZ helped in the modeling work and took part in data analysis. AM analyzed the samples by FTIR spectroscopy. TH and DC prepared the fiber and plastic materials, characterized them.

Acknowledgments

I would like to express my deepest gratitude to my advisor Dr. Ezra Bar-Ziv for his guidance, support, and encouragement. Extensive discussions with him not only helped me understand the research topic well but also inculcated in me the process of critical thinking. I would like to thank Dr. Jeff Naber, Dr. David Shonnard and Dr. Jordan Klinger for serving on my committee and reviewing the work. I would like to thank Dr. Armando McDonald for his help with characterization experimentation of bio-oils. My special thanks go to Stas Zinchik for his valuable suggestions and motivation and Zhuo Xu for all the help in lab experimentation. I would like to conclude by thanking my family and the friends for all their support and motivation.

Abstract

The main objective of this work is to investigate fast pyrolysis of fiber and plastic feedstocks in order to understand the synergistic effect from their co-pyrolysis. In this on-going work, fiber, plastic and their blend are characterized and pyrolysis oil is produced from them in the fast batch pyrolysis reactor. Based on a heat transfer model it is shown that results of oil produced from batch reactor will be applicable to the continuous paddle reactor. From feedstock characterization, chlorine was observed particularly in the plastic feedstock. Thus, chlorine removal method using torrefaction and high shear mixing was implemented and was found to be effective for chlorine removal.

The fiber and plastic pyrolysis oils produced in the batch reactor were characterized in detail using analytical techniques like GC-MS, FTIR, ESI-MS and HPLC to investigate the various compounds. It was found that pyrolysis oil produced from fiber/paper showed two different fractions with top fraction mostly consisting of cellulose and bottom fraction consisting of lignin. For pyrolysis oil from plastic, it was found that it had 60-65% compounds like the diesel fuel.

1 Introduction

1.1 Motivation

The continuously increasing demand for energy, the declining fossil fuel deposits, national security, and environmental issues such as global warming and higher air pollution levels demand the shift towards renewable fuels. We, as engineers, need to develop a cleaner, safer, sustainable, and renewable alternative for fossil fuels. Conversion of non-food biomass feedstock has been proposed for the generation of such fuels using thermochemical processes [1].

Thermochemical conversion to produce various fuels can be achieved using various pathways like torrefaction, pyrolysis, and gasification [2]. Of which, fast pyrolysis is a special pathway that attracts significant attention as it results in a liquid fuel with high energy-density. These liquid fuels can be produced from largely abundant feedstocks like municipal solid wastes (MSW), forest thinning biomass, and agricultural wastes [3–5]. As per 2016-billion-ton report, an abundance of these feedstocks can be seen from fact that availability of biomass just from agricultural and forest resources was about 343 million in 2017 which is predicted to rise to 1.2 billion tons by the year 2040 [6]. If the energy crops like soybean, cottonseed and sesame are included as feedstock, they will add another 411 million tons by 2040 [6], totaling ~1.6 billion tons. These statistics of the abundance of feedstock suitable for fuel production process, encourage their thermochemical conversion.

From the regulation perspective, energy independence and security act (EISA) developed to promote the use of domestic biofuel and to mitigate oil pricing, published renewable fuel standards (RFS-2) in the year 2007. This RFS-2 standards not only

expanded the quota for use of renewable fuels from 7.5 billion gallons (2012) to 36 billion gallons (2022) but also put restrictions on types of bio-fuels allowable in the quota. This caps the share of conventional biofuels derived from conventional feedstocks like corn to 15 billion gallons [7] and mandates the share of advanced biofuels to be increased to 21 billion gallons with at least 50% reduction in greenhouse gases. Of these 21 billion gallons of advanced biofuels, 16 billion gallons should be from ***cellulosic*** sources. In addition to RFS-2 standards, states like California under California code of regulations (Title 17) have adopted their own stringent norms for fuel sources, mandating 3% of fuel to be from low carbon sources by end of 2017 and minimum of 10% reduction in carbon intensity for fuels to be sold after 2020. Conforming to all these norms and goals of large fuel production require significant advancement in technology for thermochemical conversion.

Apart from the regulations, US is now facing the challenge of ever-increasing amount of plastic waste being accumulated in landfills due to the changing lifestyle over years. For the last several decades, it was shipped to China [8]. However recently, the Chinese Ministry of Environment and Environmental Ministry of Commerce, declared that the country will stop receiving the 24 types of solid wastes which will be extended to several more by 2019 [9]. This will induce a severe stress on the waste management industry that has no real solution to address the issue. Pyrolysis of these diverse types of plastics with biomass wastes together to produce liquid fuels using a process called co-pyrolysis can be a promising option as it also resolves associated challenges like plastic separation or plastic-biomass separation that can be expensive and labor intensive.

Out of the above potential types of feedstock, we selected to study municipal based solid wastes, mostly plastic, and fibers. As per statistics, the amount of fiber and plastic wastes recovered in the U.S. per annum are 50.8 million tons [10] and 33.25 million tons [11] respectively. Based on a 50% mass yield, these two waste streams together could, in principle, produce 15.1 billion gallons of liquid transportation fuels [12,13].

1.2 Background

Pyrolysis is the thermochemical process of degradation of biomass or waste by subjecting it to temperature range ~ 500 °C in the absence of oxygen [14]. This process results in the formation of fractions in solid, liquid and gas phase; the solid fraction is often referred to as biochar. The liquid fraction obtained by condensation of the pyrolytic vapors results in liquid and is referred to as bio-oil or pyrolysis oil. This bio-oil should be upgraded in an oil-refinery or bio-refinery for the use of transportation fuel [15–18]. It can also find its direct use as fuel for boiler burners [19]. The vast majority of pyrolysis studies dealt with biomass as the feedstock. It has three main components, hemicellulose, cellulose, and lignin. One of the feedstocks that we will study is fiber waste, which is mostly cellulose. We will discuss very briefly in this section biomass pyrolysis as it also relates to the degradation of cellulose. The next section will be devoted entirely to pyrolysis of fibers and plastics.

The products distribution from biomass pyrolysis process is largely dependent upon the heat transfer rate [14,20] and the operating conditions such as temperature and the residence time [2,21] as summarized in Table 1. The table shows the liquid, solid, and gas yields from slow and fast pyrolysis. Slow pyrolysis occurs at <400 °C and has a very slow

heating rate of a few degrees per minute yields very low liquid product (~30%), with large water content, very high char yield (~35%), and very high gas yield (~35%). On the other hand, fast pyrolysis requires heating rates of ≥10 °C/s with liquid yields of up to 75% (with low water content), low char yield (~12%) and low gas yield (13%). In fast pyrolysis, the liquid production will spend short residence times (~ 2 sec) to avoid secondary reactions [20] before condensation. Clearly, slow pyrolysis is highly desirable for obtaining quality liquid product and high yields. The pyrolysis community is thus converting organic feedstock by fast pyrolysis only.

Table 1 Typical parameters and product yields for different types of pyrolysis [20,21].

Type	**Temperature (°C)**	**Residence time (s)**	**Typical Yields (%)**		
			Liquid	**Char**	**Gas**
Slow pyrolysis	>400	hundreds	30 (~70% water)	35	35
Fast pyrolysis	~500	10-25	75 (~25% water)	12	13

Bio-oils composition resulting from fast pyrolysis process can be composed of different molecules of various sizes derived primarily from the process of depolymerization of three key building blocks of biomass namely cellulose, hemicellulose and lignin [22]. The exact composition is dependent on various factors like the temperature of fast pyrolysis process, heating rate, vapor residence time and the type of feedstock used [20,22–24]. According to Mohan et al. and Branca et al. [25,26] pyrolysis oil (bio-oil) is a complex mixture of a variety of around 300 compounds. However, majority of authors [22] report only a few major compounds like acetic acid, formic acid, propanoic acid, 2-furaldehyde, levoglucosan, glucose, xylose, methyl-cyclopentenone, methanol, phenol, butanedial, etc. It is reported that acetic acid is a principle acidic compound observed in the bio-oils and

furfural and furfural-alcohol are major furan products observed. Most of these compounds are the product of fiber pyrolysis as well.

Because of such large variety in compounds stated above, various analytical methods are used to characterize the bio-oil. Chemical characterization of oil is done based on the chemical functional groups with the use of solvent extraction, molecular distillation, etc. More advanced chemical characterization methods like GC-MS, TIC, HPLC, GPC are used to focus on different aspects needed for the study [26–29].

1.3 Literature review

This work focuses on pyrolysis of solid waste blends that comprise fiber and plastic materials. The fiber being mostly cellulose with some minerals as fillers [30] and the plastic being a large number of plastic polymers. In the research, we will study each of the components separately (i.e., fiber and plastic alone) and their blends.

There are few studies on pyrolysis of fibers, plastics, or their blends [3,31]. Out of these limited studies, there are fewer pyrolysis studies on fiber-plastic blends – referred to as co-pyrolysis. During co-pyrolysis, the presence of synergistic effects between different wastes has been implied recently by researchers [32,33]. If synergistic effects are absent between fiber and plastic, the yield and properties of the various components should be the weighted sum of the two reactants. However, the actual yield from the co-pyrolysis may be different, if it is below the average, it is negative synergy, if it is above the average it is positive synergy.

Synergistic effect has been studied mainly in two categories: (i) type of pyrolysis, and (ii) catalytic pyrolysis. The current literature review focuses mostly on non-catalytic

type slow and fast co-pyrolysis of fiber (cellulosic) with different types of plastics. However, as cellulose (fiber) is a major component of biomass, which has a primary structure of two β-glucopyranose units linked by β-1,4-glycosidic bonds [34], a few references to biomass-plastic co-pyrolysis are also used in order to understand cellulose-plastic synergy.

The following paragraphs deal with ***slow co-pyrolysis***: Sharypov et al. [32] experimented with co-pyrolysis of various biomass-plastic combinations using biomass feedstocks of pine, cellulose, and lignin with plastic feedstocks of medium density polyethylene (MDPE), atactic polypropylene, and isotactic polypropylene in an autoclave. Their results demonstrated that 400 °C was the ideal temperature for maximum light liquid yields and that polyolefins thermally degraded at higher temperatures as compared to the biomass feedstocks. Significant synergistic effects were seen when the biomass-to-plastic ratio was lower than unity resulting in a higher liquid percentage. Yuan et al. [34] studied synergistic effect during co-pyrolysis of cellulose and high-density polyethylene (HDPE) at various ratios for two decomposition phases: cellulose phase and HDPE phase and found that mass loss values of mixture were greater than the estimated values confirming synergy and proved that synergy was strongest when cellulose-to-HDPE ratio was 1:3. Also, study by Gunasee et al. [35] using cellulose and low-density polyethylene (LDPE) plastic, found that positive synergy increasing liquid yield existed under both devolatilization and condensation conditions. Wang et al. [36] studied the synergistic effect demonstrated in blends of polylactide (PLA) and various biomass types and found temperature regions showing most effect based on the overall devolatization. Brebu et al. [37] co-pyrolyzed

pine cone and polyethylene (PE), polypropylene (PP) and polystyrene (PS) types of plastic at 500 °C and found that gas and liquid yields increased while char yield decreased. Overall, key factors identified that affect synergy in co-pyrolysis of fiber-plastic are type of feedstock and mix-ratio, pyrolysis duration, and reactor temperature [38].

Slow co-pyrolysis of cellulose and plastic is proved to be providing beneficial effects not only in terms of product yield but also on the quality of oil produced. Önal et al. [39] performed co-pyrolysis of the almond shell and HDPE plastic at 500 °C in a fixed bed reactor and reported a synergistic effect on both yield and composition. They concluded that there was a positive synergistic effect of higher HDPE amounts resulting in positive synergy, an increase of 26% in Higher Heating Value (HHV), 26% in carbon content and 78% in hydrogen. These positive synergies are consistent with the negative effect observed for oxygen (86% reduction). Chen et al. [40] co-pyrolyzed waste newspaper and HDPE plastic in a stationary furnace setup and found synergistic effect between temperatures in the range of 400 – 500 °C and observed increased yield, decreased viscosity and a significant decrease in total acid number (TAN) compared to theoretical data.

Apart from the mentioned traditional feedstock (biomass) and reactors (circulating fluidized bed), researchers also tried using different feedstock like tires and methods like auger reactor for co-pyrolysis with biomass. Martinez et al. [41] conducted a study of forest waste and waste tires using a fixed bed reactor and an auger reactor separately to compare the effect of type of reactor. They not only found positive synergy between the waste tire and biomass co-pyrolysis but also showed it is more evident in the case of auger

reactor. Further, it was also found that addition of tire waste in this co-pyrolysis increased the stability of the oil showing effect on quality.

Yet, along with mostly positive synergistic effect resulting studies, some literature studies also showed negative synergistic effects in slow pyrolysis. Williams et al. [42] investigated yield and composition of co-pyrolysis of oil from fiber-polysterene in a fixed bed reactor using catalyst and found a decrease in the oil and significant increase in the formation of coke. Meng et al. [43] studied co-pyrolysis of polypropylene and sawdust in a packed bed reactor to understand the effect of temperature on yields and found a negative synergistic effect in co-pyrolysis. According to Xue [44], possible explanation for some of these negative synergistic effects is that the plastic decomposes at a higher temperature than biomass but melts at around 300ºC which is approximately the decomposition temperature for biomass. Due to this overlap, it is likely that biomass gets covered in the melted plastic and thus hindering the process of effective mass transfer. This may induce secondary reaction like decarbonylation and thus increasing solid products generated from accumulation and retention of solids from biomass and plastics leading to a negative synergy.

The following paragraphs deal with ***fast pyrolysis***: Comparatively much less work has been done on fast co-pyrolysis. Ojha et al. [33] studied the effect of cellulose-plastic mass ratio and pyrolysis temperature using a micro-pyrolyzer. They found that alcohol content increased as the ratio of PP plastic in the PP-biomass mix increased. Contrast to normal, the char yield showed positive synergy in fast pyrolysis which is a more common phenomenon in slow pyrolysis instead. It was attributed to reaction of PP derived vapors

with biomass char and then subsequent production of aromatic ring compounds that were retained in char in solid form. Chen et al. [45] studied fast pyrolysis of Paulownia (PAW) wood and PET plastic using drop-tube fixed bed reactor and found increased experimental gas yields compared to theoretical yields with an increase of temperature and PAW mass ratio. Burra and Gupta [46] co-pyrolyzed pinewood with different kinds of plastics like PP, Polyethylene terephthalate (PETE), and polycarbonate (BPC) and found that co-pyrolysis synergistically reduced the char yield. Chattopadhyay et al. [47] and Çepelioğullar et al. [48] showed the gas yield was increased and char was inhibited while Xue et al. [49], Yang et al. [50], Ko et al. [51] studies showed that gas yield was inhibited in the co-pyrolysis. Further, Sanchez et al. [52] showed that no synergy effect in present on gas yields in pyrolysis and they act as independent systems. This variety of outcomes from various studies demand a better understanding of the synergy effect phenomenon in fast co-pyrolysis.

As indicated above, from both slow and fast co-pyrolysis, there are discrepancies between the various studies and it is not clear what are the sources of these discrepancies. As synergy may play an essential role in the product yields and their properties, it is of great importance to study the existence of synergy in co-pyrolysis. In order to study synergistic effects, in co-pyrolysis one has to ensure that the reactors used would enable studying these effects. The main reactors used in fast pyrolysis are based on circulating fluidized bed (CFB) reactors [14]. Recently the MTU group has developed a paddle reactor that yieled the same yields as CFB [53], however, it is much simpler and at signficantly lower cost. This reactor will be used in this study.

1.4 The paddle reactor

In auger reactor and paddle reactors pyrolysis (described in detail in 3.2.2), the feedstock is continuously fed to a screw/paddle and rotation of screw moves the product to the end of the screw through various heating zones. They are gaining popularity because of their simplicity of construction and operation [53]. These reactor also need little or no carrier gas thus reducing operational needs. The process can be very easily controlled by just controlling the rotation speed [53]. Also, because of its small footprint compared to CFB the capital cost is also reduced. However, at large scales heat transfer in auger/paddle can be a challenge [54]. Also, there is no simple strategy for scaling them up to industrial size [55] prompting for more research work.

This study focuses only on paddle reactors (described in detail in 3.2.2) for fast pyrolysis as they previously proved to be good mixing devices in continuous flows of powders with the extremely simple operation and low cost. Much work has been carried out to study mixing in various paddle configurations. Hassanpour et al. [56] modeled a paddle mixer by a discrete element method (DEM) to analyze the particle motion within the reactor. He described internal flow fields and mixing patterns and obtained good agreement with measurements, indicating that DEM is an appropriate tool for predicting particle dynamics in these mixers. Bohl et al. [57], characterized powder mixing in a paddle reactor by measuring flow velocities and comparing them with modeling results using finite time Lyapunov exponents. Recently, Pantaleev et al. [58], carried out the most comprehensive investigation on paddle mixing that included measurements supported by

DEM simulations, which used the visco-elasto-plastic DEM model developed by the same team [59].

Although paddles are widely used as mixing devices, surprisingly very few attempts have been made to use them for reaction. Rui et al. [60], carried out for the first time high-temperature reaction in a paddle reactor in the year 2012. They studied fast pyrolysis in the temperature range 450-550°C. However, it is of interest to note that screw augers have been used extensively as high-temperature reactors, (for pyrolysis by Day et al. [61,62]; Aylón et al. [63]; Martinez et al [41]; Miao et al. [64]; Haydary et al. [65]; Butler et al. [66]; and for gasification by Chun et al. [67]. The common way for heating is externally (Garcia-Perez et al. [68]; Kelkar et al. [69]; Ingram et al. [70]; Mohan et al. [25]; Pittman et al. [71]). The main disadvantage of screw augers as high-temperature reactors is the slow heating rates (<1 °C/s), which is not suitable for fast reactions such as pyrolysis with characteristic times of 1-3 seconds. Recently, Funke et al. [55,72,73] carried out a comprehensive study on the use of twin screws for fast pyrolysis including up-scaling considerations.

A logical approach is to combine the simplicity of the heating method developed for simple screw augers with the outstanding mixing portrayed by paddle mixers and use of externally heated paddle mixers for continuous fast reaction systems. This might yield in fast heating rates for continuous reacting systems. As described in previous paragraph, in such reactors particles of various diameters are flown and heated by the hot reactor walls and react to produce solid, liquid, and gaseous products. Our research group has already developed an externally-heated paddle mixing reactor (1-inch inner diameter of the paddle

housing with a throughput of 100-1,500 g/h). We discovered that to reach the desired high heating rates, the shaft where paddles are attached should rotate at frequencies at or above 200 rpm. Using this reactor, comprehensive pyrolysis study of about 20 different types of feedstock showed that the product compares well with literature data that were obtained for fast pyrolysis reactors [53,74]. As essential parameters like heating rate, flow rates and method of mixing are well understood from one-inch system.

2 Research objective

Based on literature reviewed on synergistic effects during pyrolysis between fiber and plastic materials, both slow and fast co-pyrolysis show discrepancies between the various studies and it is not clear what are the sources of these discrepancies. As synergy may play a crucial role in the product yields and their properties, it is important to study the existence and the extent of synergy in co-pyrolysis. The primary objective of this work is to study these synergistic effects, in co-pyrolysis of fiber-plastic. Prior to the study of synergistic effect in fiber-plastic blend, the individual constituent feedstocks fiber and plastic will be investigated independently.

The specific objectives of the proposal are to investigate:

1. The kinetics and product distribution in fast pyrolysis of fiber and plastics.
2. The effect of chlorine and other minerals on fast pyrolysis of fiber and plastic (minerals may result in formation of large amount of lower molecular weight species making upgrading difficult [75]).
3. The synergistic effects in fast co-pyrolysis of fiber-plastic blends under the following conditions: (a) with/without chlorine and minerals (b) at various fractions of fiber/plastic in the blend, in the range 0.1-0.9.

To achieve these goals we will use two types of fast pyrolysis reactors:

1. A batch reactor that we developed for fast pyrolysis, where the majority of the experiments will be conducted. This will provide a large data base as these experiments are rather simple and inexpensive. In these expeiments a sample of

~20 g material is inserted into the batch reactor and the liquid products are condensed and collected.

2. A continuous fast pyrolysis paddle reactor that can produce ~8 gal/hr liquid product. To minimize the numbers of experiments in this reactor, we will use the batch experiments to provide the pyrolysis parameters and the fiber-plastic blend to be tested.

The following parameters will be used to quantify synergy: (1) liquid yield; (2) pyrolysis char, (3) water content in liquid; (4) gas yield; (5) H/C ratio in the liquid yield; (6) oxygen content in the liquid yield; (7) average molecular weight in the liquid yield; (8) aromatic molecules; (9) CO; (10) CO_2. Other compounds might be: Levoglucosan, saccharides, acetic acid, lactic acid, epoxide, alcohols, ethers, phenols, furans, ketones, esters.

3 Materials and methods

3.1 Feedstock material

Figure 1 (A-D) illustrates the feedstocks that will be studied: (A) fiber waste; (B) plastic waste; (C) loose fiber-plastic blend; (D) densified fiber-plastic blend.

Figure 1 CE feedstocks (A) fiber/paper (B) plastic (C) loose fiber-plastic waste-blends (D) densified fiber-plastic blend pellets.

The wastes received by CE comprises of a large variety of paper, matrix residuals, laminated papers, plastics, and fibers consisting of several chemical impurities (see below in Section 5.1). The following are major obstacles in dealing with thermal treatment of organic wastes:

- Presence of metals that need removal as they might be hazardous or/and damage the equipment.
- Moisture content that can vary from batch to batch.
- Variety in component distribution in the waste.
- Hazardous heavy metals present.
- Existence of hazardous chlorine and potassium needs handling.
- A large size distribution that affects heat and mass transfer during the process.

Following are the common methods that provide solutions that best fits the needs for the obstacles discussed above.

- For metal removal, the waste is first shredded to 3-5-inch size particles by a shear grinder. Ferrous metals are sorted, completely, by strong electro-magnets while non-ferrous metals are removed by manual sorting which is currently best method based on industry practice.
- For moisture content, exceeding 7%-mark, natural indoor drying by spreading it on the storage floor is used as it requires very inexpensive structures.
- Variability of feedstock primarily affects two key things: (a) consistency of product in terms of parameters like heat content (b) biogenic carbon content in product (if required by norms). As, our feedstock primarily consists of fibers and plastics this challenge is addressed by characterizing the incoming feedstock and comparing it with the desired product properties. If the biogenic carbon needs to be boosted fibers percent is increased while for heat content more plastic is added.
- As for the hazardous materials, this study does not use industrial waste that cannot be treated for energy applications. Also, it does not contain high content of heavy metals. These are commonly treated in special facilities at very high costs.
- Feedstock with large chlorine and potassium content are treated with an efficient and economical method where these components are removed in aqueous solution after torrefaction discussed below in Section 3.2.3.
- As most thermal processes require particles to less than certain size (6 mm for this work). The feedstock is shredded/grounded using a hammer mill to < 6 mm size

ensuring unhindered heat and mass transfer in the reactor.

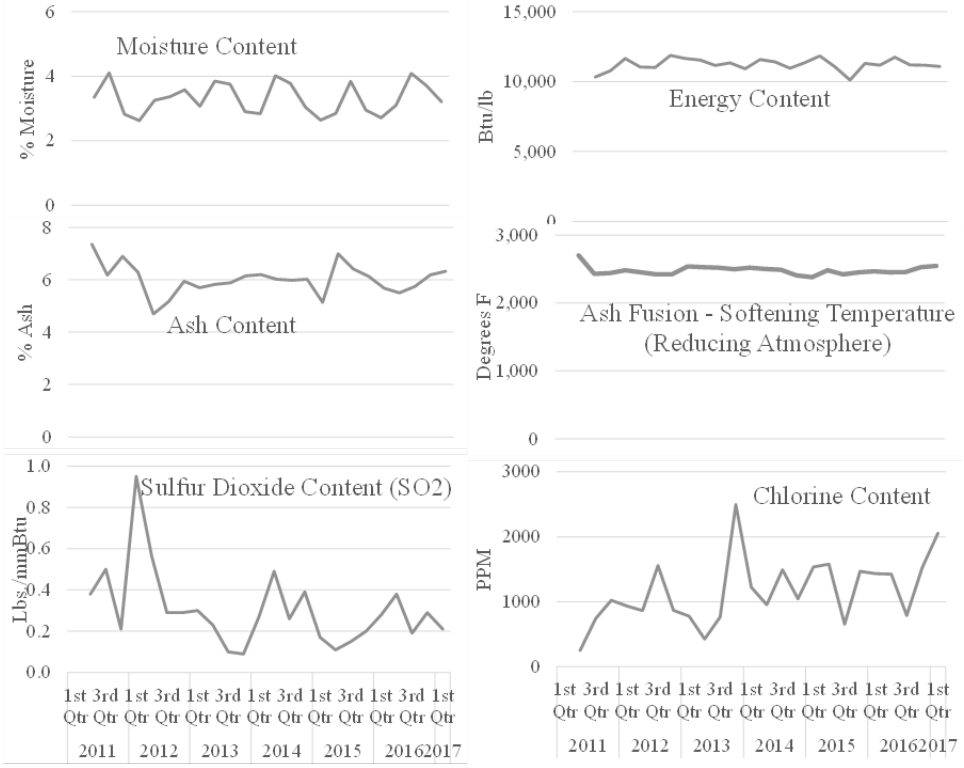

Figure 2 Feedstock characterization on quarterly basis from year 2011 to 2017 by CE.

Above described methods have resulted in highly consistent and uniform feedstock material. Figure 2 displays some of the properties of fiber-plastic blends for a period of seven years' time that addresses the criteria set above. As seen from Figure 2, moisture content and ash content are stable at ~3% and 6% respectively. Energy content is stable at 26 MJ/kg. SO_2 is in average under 0.3 lb/mmBtu, except on one occasion but is always under permitted values. Mercury is in average 0.009 ppm, except two occasions but is well under the EPA permitted values of 0.065 ppm. However, the main pollutant emission that is above EPA permitted value is chlorine, in the range 254-2497 ppm (average of 1162±486 ppm), well above the EPA permitted value [76]. Thus, it is addressed separately in this

methods section. Overall, CE's method provides rather consistent and uniform material. The characterization results are reported in section 5.1.

3.2 Methods

3.2.1 Batch pyrolysis

Batch pyrolysis was performed using a lab setup as shown in Figure 3. The setup consisted of following key components: (a) a Lindenberg furnace (Model: Lindenberg/Blue type BF51828C-1) for heating the feedstock, (b) a metal container for pyrolysis (c) a heated transfer line to avoid condensation in (d) a bottle for oil collection (d) cooling system consisting of a fan (not shown) and water bath for collection bottle.

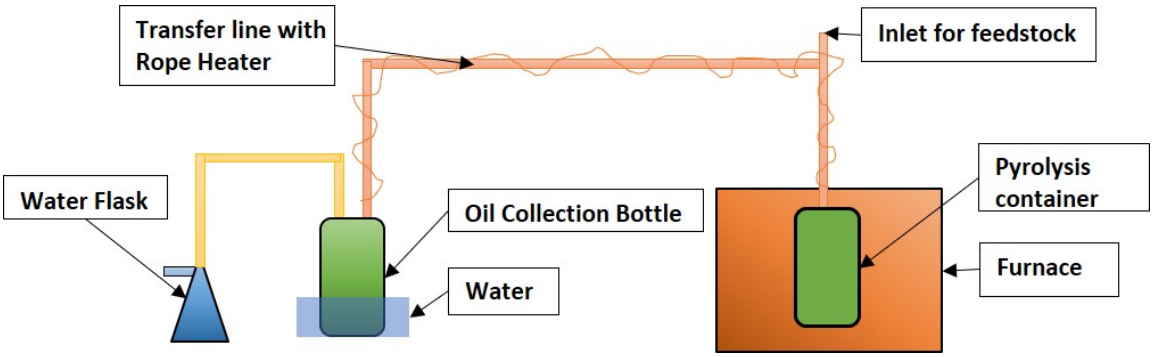

Figure 3 Batch pyrolysis schematic.

The batch pyrolysis experiments to produce oil samples were performed using the following procedure: The fiber-plastic feedstock to be used was weighed using electronic scale (model A&D EK-15KL) with readability of 0.1 g. The entire assembly was also weighed to conduct mass balance to account the weight of any oil condensed in the transfer line. The furnace was set at temperature of 500°C and the transfer line was heated to 250 °C to avoid condensation of pyrolytic vapors in transfer line. The transfer line and heater

were covered with insulation to avoid loss of heat to surrounding. The temperatures were measured using a J-type thermocouple and controlled using a controller. The temperatures were allowed to reach steady state before the start of experiment. The collection bottle was then weighed, and liquid collected was measured using weight difference at the end of experiment.

During the experiment, the inlet for feedstock was opened and 5 to 10 grams of feedstock was dropped inside the container/bomb and inlet was sealed back. The vapors formed from pyrolysis of the feedstock would travel through transfer line to the condensation system and would condense in the form of liquid due to the water bath of collection bottle and fan. The non-condensable vapors would be released from the system in form of bubbling in the water flask. The bubbling started ~2-3 seconds after the material dropped inside the pyrolysis container. New fiber/plastic feedstock was added approximately 5 minutes after the bubbling stopped. At the end of experiment, the collection bottle was weighed to measure the liquid yield. The char was measured using the weight difference of the bomb before and after the experiment. The liquid condensed in transfer line that did not reach collection bottle was measure using weigh difference of transfer line and was added to the liquid yield.

The batch experiment is a simple experiment that requires less time and operational cost as compared to the paddle reactor system and can provide oil from fast pyrolysis required for further testing. To prove that the batch pyrolysis is indeed fast pyrolysis, heat transfer analysis was performed on the batch reactor system. The details of the analysis are shown in the 5.2.1 section.

3.2.2 Continuous paddle reactor pyrolysis

We are currently building a 4-inch system for this thesis work. However, MTU developed, designed, tested, and operated a 1-inch system that is similar to the current 4-inch system [77]. This 1-inch system was shipped to Idaho National Lab (INL) and is operated by INL. Some recent experiments were performed in the 1-inch system al INL. This section consists of some design aspects and results for the 1-inch system; followed by some details on the 4-inch system that is currently in assembly stages.

The key component of the continuous paddle reactor is the reactor with the mixing element. Our paddle mixer comprises of two mixing elements: (A) cuts in the auger flighting and (B) four mixing paddles within each flight pitch. We found that these features to enhance significantly mixing. The reactor diameter is 2.54 cm with a pitch of 5.08 cm and a shaft diameter of 1.27 cm. The flighting cuts consist of five-equal length segments of spacing of 36 degrees each.

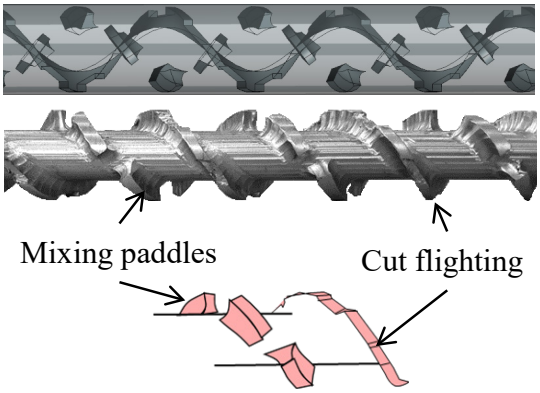

Figure 4 Paddle reactor schematic.

Figure 4 shows the reactor configuration and its features. Within the 36° of the flight, ~40% of the flighting area is cut away leading to some material not being conveyed

forward and mixing it with the new materials coming in from the previous pitches. In addition to the flight, four paddles were also placed within each pitch to push the material both forward and on sides and to lift and retain the solids. The paddles are placed at 45° to the shaft. They work as an internal mixing device within each pitch. The paddles have of similar size to the flighting cuts but extend from auger shaft to the same diameter as the normal flighting. Four paddles are placed in each pitch with even spacing in between them. Cut flighting's and paddles improve solids mixing.

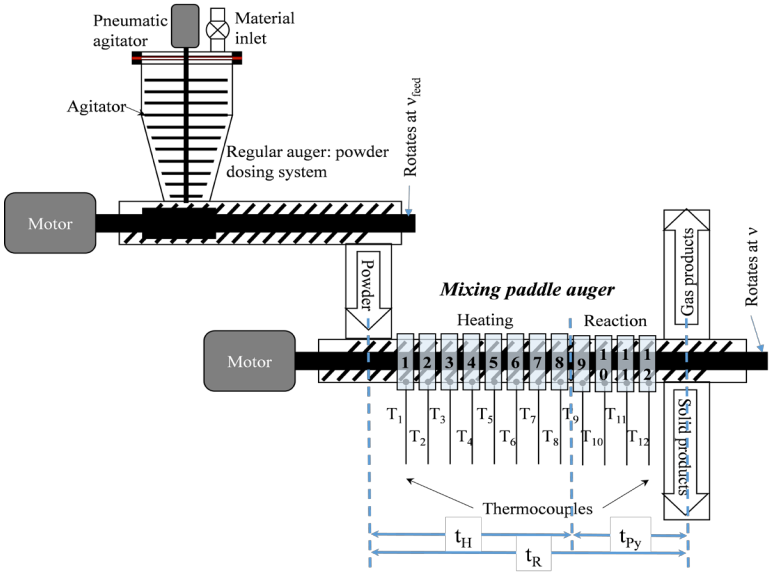

Figure 5 Cartoon of paddle reactor system.

Figure 5 shows a cartoon of our paddle reactor system for fast pyrolysis. The feedstock will flow into an agitated feed bin (to prevent bridging) and is flood fed into a screw auger. The feedstock falls into our paddle reactor that is heated by twelve heaters, with a thermocouple for each heater that measures the powder temperature at the reactor floor. Each heater has power larger than the heat rate required to heat all powder to the required temperature. The heaters are covered by insulators that does not lose more that

5% heat to the surroundings. The thermocouples are used to control the power of each heaters as required.

Figure 6, right, shows the heating dynamics and behavior in the 1-inch system in a two-stage heating mode. The temperature along the axial axis of pyrolysis reactor was set such that Heaters 1-4 would be at 350 ˚C (at 350 ˚C negligible pyrolysis reactions occurs), whereas Heaters 5-12 were set at 500 ˚C, where pyrolysis takes place. All heaters were controlled according to the set points. Figure 6-Left shows the temperature vs. time curve for heaters 1, 4, 5 and 10, from the beginning of the heating. After the system is turned on, it takes ~700 s for the system to reach a steady state after the initial surge due to system thermal capacity. The material is then introduced at ~1300 seconds which causes a drop in the temperature, however system recovers in few tens of seconds and achieves the steady state again as the feedstock reaches the heater temperature. From the heater 4 to heater 5 there is a jump in the heater set temperature from 350 to 500 °C as a result temperature at thermocouple 4 and 5 always lie between these two temperatures.

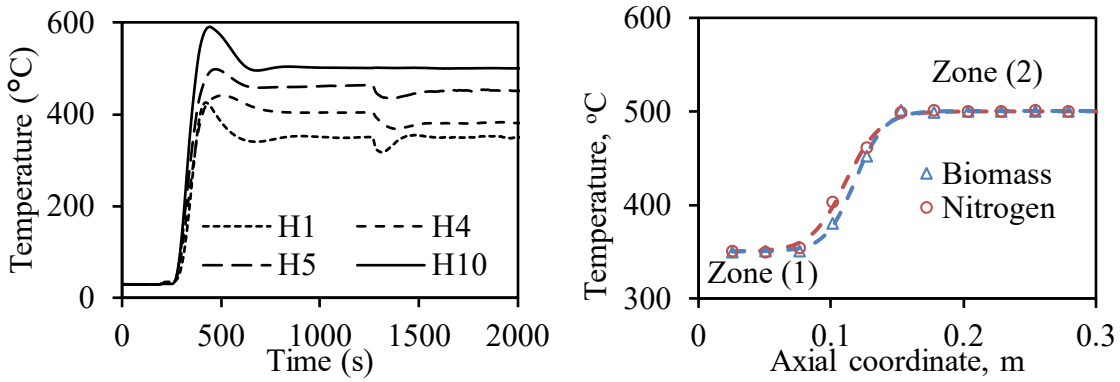

Figure 6 Left - Temperature profiles for heater 1, 4, 5 and 10 in 1-inch system. Right - Temperature distribution vs. axial co-ordinate for 1-inch pyrolysis system.

The temperature vs. axial distance for two materials: (1) biomass (2) pure nitrogen was plotted as seen in Figure 6-B, A S-shaped curved is formed showing the thermal behavior of heaters. For the 4-inch system, similar thermal behavior is expected, with difference only being with higher thermal capacity, thus requiring longer times to reach steady state required.

Apart from heating methods for main pyrolysis reactor described above, system consists of separate collection system for products, solid, liquid and gas. The gas stream consisting of condensable bio-oil and non-condensable gases flows through a heated transfer line. It is then passed to a condenser that collects the produced liquid into a sealed tank (not shown**Figure 7**). The cold non-condensable gases are then passed through a cold-water bath to collect any remaining bio-oil. The system is kept inert with a nitrogen stream. In order to avoid the secondary reactions, the nitrogen flow rate is set such that residence time of gases do not exceed 2 seconds.

The 4-inch system is shown in Figure 7. It consists of a bucket elevator which transfer the feedstock to the hopper feed-bin consisting an agitation system to avoid any kind of bridging in the feed-bin hopper. The feed is then supplied to the reactor through an air-lock which ensures the reactor stays in oxygen-free environment. All the pyrolysis reaction take place in the reactor shown in Figure 8 which consists of a paddle auger (refer Figure 8-A) to enhance mixing as well as higher heat transfer similar to the 1-inch system. The heating is achieved using 15 band heaters. The temperature is monitored and controlled by 24 different thermocouples approximately spaced 2-inches for each other.

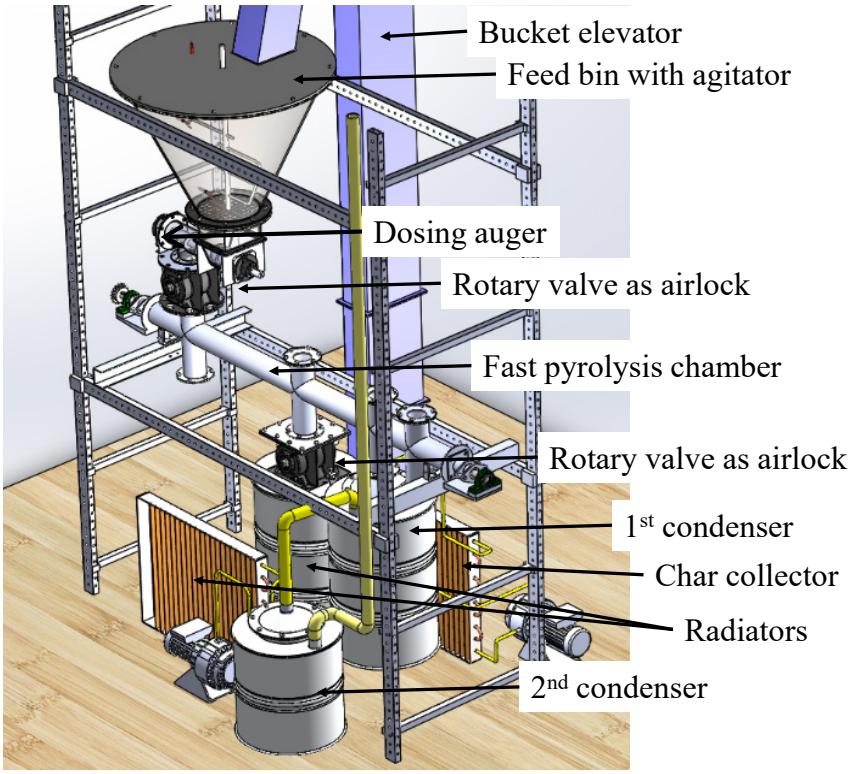

Figure 7 Solid-works model showing the design of 4-inch continuous paddle reactor system.

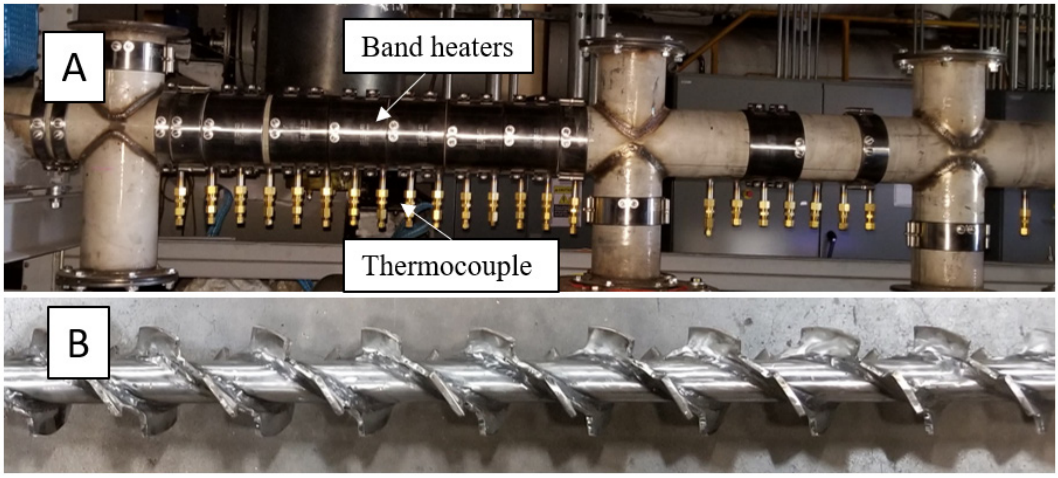

Figure 8 (A) The 4-inch reactor showing band heaters and thermocouple connections (B) Reactor paddle shaft.

3.2.3 Chlorine removal

Waste blends of plastics often contain chloride containing plastics, like polyvinyl chloride (PVC) and polyvinylidene chloride (PVDC). Based on study by Saleh et al. [78],

it is known that chlorine from these plastic materials is released in the form of hydrochloric acid when it is torrefied at 300 °C. This acid may damage pyrolysis reactors and add cost of hydrogen chloride or dioxin removal in aftertreatment [79].

Traditionally, leaching is used as a method for mineral removal which uses large quantities of acids for soaking/washing along with significant amount of processing time and corrosive effluent treatment [74]. Based on method developed by Donepudi [74], Chlorine removal in this study was done by use of torrefaction and high shear mixing, as follows.

Torrefaction. Torrefaction involved heating the sample in oxygen-free environment at 300°C. Typically, a sample of around 150 g was used. Torrefaction experiments were carried out at using convection type furnace manufactured by Lindenberg (Model: Blue type BF51828C-1). The oven was preset at 300 °C and was allowed to stabilize at the same temperature for ~15 minutes. The furnace was then filled with continuous supply of either N_2 or CO_2 gas to avoid oxidation of the sample during the torrefaction. Once the temperature and the gas flow were stabilized, the weighted sample was placed in a pre-weighed aluminum foil tray in the center of the furnace. For the fiber-plastic blends the sample weight was ~300 g and the residence time of the sample varied from 3 to 120 minutes.

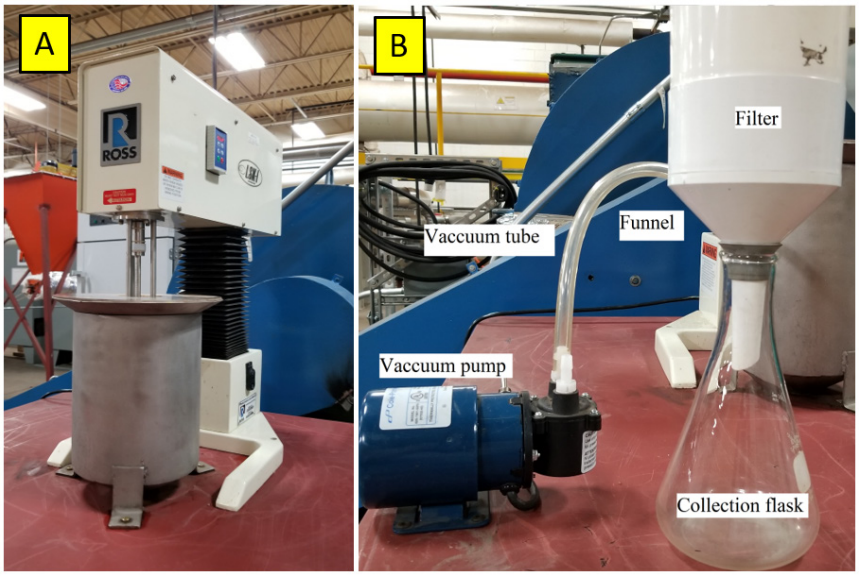

Figure 9 (A) Charles Ross & Son Company's (Model HSM-100-LSK-1) high shear mixer used in chlorine removal. (B) Chlorine filtration setup.

High shear mixing. A Charles Ross & Son Company high shear mixer (Model HSM-100LSK-1) as shown in Figure 9 was used for high shear mixing. The mixer has speed range of 500 to 10,000 rpm. The mixer mixes the torrefied sample fiber-plastic and water vigorously for a specified amount of time to form a homogeneous slurry. The slurry is then filtered using a Whatman filter paper and a vacuum pump. The separated products are weighed, and the water washing is collected separately for the Chlorine analysis described in section 4.6.

4 Characterization

4.1 Proximate analysis

As composition of feedstock has a significant effect on properties of oil generated in fast pyrolysis, it is important to characterize physical properties [24]. Table 2 summarizes the physical properties and their effect on: the pyrolysis process, upgrading and, the final product. The measured values of these properties are presented as a part of proximate analysis section in Table 5 in Current results section. American society for testing and materials (ASTM) standards are used for the proximate analysis of the samples. The measurement of moisture content, ash content, volatile matter, fixed carbon, and calorific value were based on ASTM E871, ASTM D1102, ASTM D3175, ASTM D3175 and ASTM E711 standards respectively. The final values are calculated based minimum 10 measurements.

Table 2 Feedstock physical attributes and their effects on pyrolysis

Physical property	**Effect on pyrolysis, upgrading and product.**
Type of feedstock	Conversion efficiency and transportation cost [24].
Moisture content	Drying, grinding energy, and feeding efficiency [24].
Energy density	Thermochemical conversion efficiency, storage cost and transportation cost [24].
Ash content	Wear and tear of handling equipment, waste handling cost, oil yield, pretreatment cost, bio-oil quality, catalyst effect on vapor cracking, phase separation [14,80–83].
Hydrophobicity	Outdoor storage suitability and drying cost [24].

4.2 Ultimate analysis

Chemical elements and the heavy metals play an important role in affecting the pyrolysis and the yield qualitatively as well as quantitatively. Thus, it is important to

understand the how these chemical compounds and heavy metals affect the process and product. Chlorine and mercury removal is more important in the pyrolysis process. However, as seen in current results section no mercury was found in feedstock, but Chlorine was found so chlorine removal method was focused separately. Various elements described in Table 3 are measured in ultimate analysis and ash content section in Current results. In the ultimate analysis the carbon, hydrogen, and nitrogen percent were measured based on ASTM standard test ASTM D5373. The oxygen content result is based on ASTM D3176.

Table 3 Feedstock chemical attributes and their effects on pyrolysis process and product.

Physical property	**Effect on pyrolysis, upgrading and product.**
Chlorine	Corrosion from HCl in pyrolysis vapor, slag formation if reacted with sodium or potassium, corrosion in combustor based on concentration [14,25,84].
Mercury	Forms poisonous vapors, cause particulate emissions, affect char use. Adds gas and oil cleanup [83–85].
Lead	Forms fly-ash and aerosols. Adds gas and oil cleanup [83–85].
Sulphur	Forms H_2S and hinders deoxygenation. Form SO_2 in exhaust and corrodes surfaces and damages catalyst [14,84].
Nitrogen	Foul odor and forms NO_x [14].

4.3 Gas chromatography - mass spectrometry (GC-MS)

GC-MS is an analytical technique consisting of an amalgamation of two different techniques namely, gas chromatography and mass spectrometry. It is primarily used for separating closely related component from a chemical mixtures and identification of mass spectrums (mass to charge ratio) of a compound at a molecular level. Figure 10 shows the block diagram of a GC-MS setup. GC section is composed mainly of an injection port, GC oven, carrier gas supply tank and regulator, and detector while the MS section consists of an electron ionization unit, magnetic lens, and an electron multiplier detector.

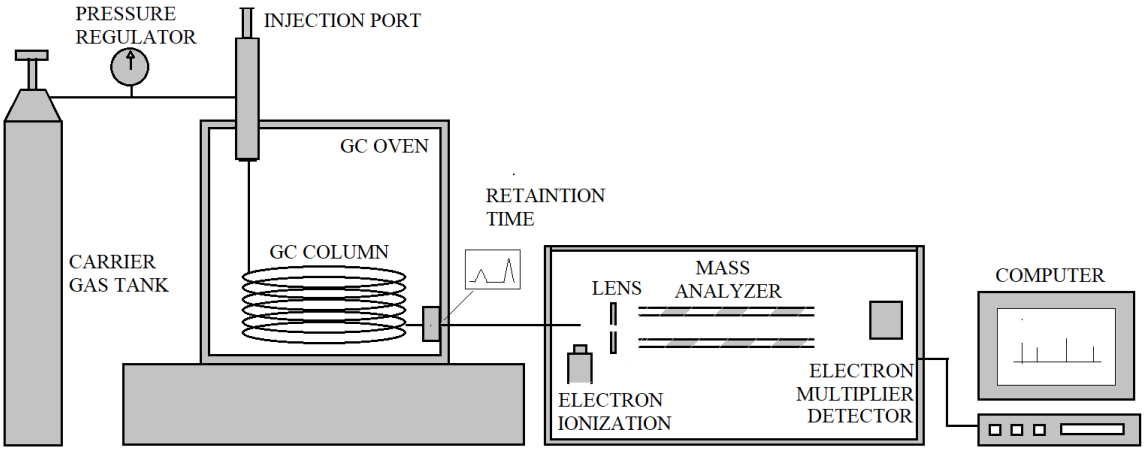

Figure 10 Gas Chromatography-Mass Spectrometry (GC-MS) block diagram.

The principle for gas chromatography is the partition coefficient caused at higher temperature flows. The detailed working is as follows: A volatile and thermally stable organic compound which is to be analyzed is mixed in solvent is injected into the chromatograph. Normally, a noble gas like helium is used to purge this mix through a GC column which is a long tube with very small diameter. For the volatilization of the sample and solvent mix, the GC column is heated in a GC oven. In the GC column, the gas forms the mobile phase while the liquid coating on solid support forms the stationary phase. The molecules and compounds soluble in the stationary phase liquid are slowed down and their emission from the GC tube is delayed. The detector at the end of the GC column records the time of arrival of each compound.

In the mass spectrometry (MS) section, the process starts with ionization of an analyte received from the GC column using the electron ionization unit. Analyte loses an electron in the process of ionization resulting in the generation of the molecular ion. This molecular ion is excited using a beam and allowed to reach a higher energy state.

Further, due to continued receival of excessive energy, the molecular ion splits into smaller daughter ions that have a lower mass to charge (m/z) ratios. The positive ions produced in the electron stream due to splitting, are then sent towards the mass analyzer which differentiates them according to their mass. These ions sorted based on their m/z ratio then hit the electron multiplier detector which generates a signal and sends it to the computer.

The computer, based on received signal, generates a graph with multiple peaks. The tallest peak is called base peak and other peaks are calculated as a percent of the base peak. For this work, GC-MS was performed using Thermo-scientific FOCUS-ISQ and anthracene was used as internal standard. Separation was achieved using a RTx-5MS capillary column.

4.4 Electro-spray ionization - mass spectrometry (ESI-MS)

Like the GC-MS system, ESI-MS system is an amalgamation of electro spray ionization and mass spectrometer. The primary advantage of ESI-MS is that it can analyze a very large range of sample compared to GC. It is more suitable for compounds with high polarity and high thermal instability. Figure 11 demonstrates a block diagram of an ESI-MS setup block diagram.

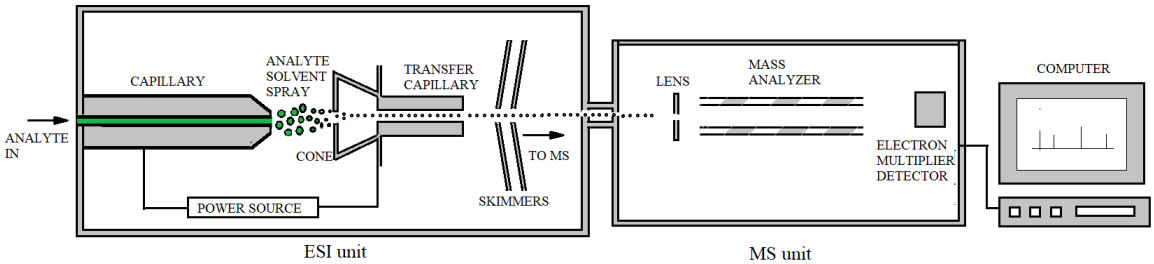

Figure 11 ESI-MS block diagram.

Electrospray ionization is used to produce ions using an electrospray from the capillary shown above, where a high voltage application produces small particles called aerosols. The analyte is forced into a capillary cone called Taylor cone using a pump at high pressure to form above mentioned aerosols. The solvent in the droplets progressively evaporates leaving analyte increasingly more charged. When charge exceeds the Rayleigh limit the droplet explodes. Due to explosion the droplet dissociates leaving a stream of charged ions. This ion stream then enters the mass spectrometer. The mass spectrometer works like MS explained in GC-MS section above.

4.5 Fourier transform infrared spectrometry (FTIR)

FTIR is used for the identification of various chemical functional groups. It was method developed to overcome the slow scanning process of dispersive instruments for chemical functional group identification. Figure 12 show a block diagram of FTIR setup. It mainly consists of four key components, namely, infrared source, interferometer, detector, and a computer for fast Fourier transform calculation (FFT).

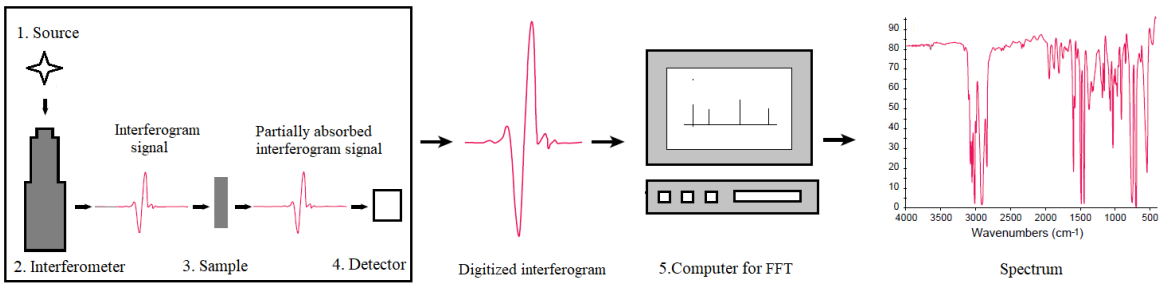

Figure 12 Fourier transform infrared spectrometry block diagram (FTIR).

The source emits an infrared beam from a black-body source. It passes through an aperture (not shown) which controls the amount of light that can reach the sample. It is

followed by an optical device called interferometer. This interferometer usually comprises of a beam splitter which divides the signal from source in two different beams. These beams are bounced off from two different flat mirrors one stationery and other moving. These bounced signals are collected behind beam splitter which produces a signal called interferogram comprised of the signal resulting from interference of two beams. It has unique property that it is composed of all the infrared frequencies.

This interferogram beam is projected on the sample. Based on the property of sample and type of analysis method, certain frequencies are absorbed into the sample. The rest are detected by a detector and final measurement is made. As frequency spectrum is needed for the analysis, this interferogram is digitized and sent to fast Fourier transform (FFT) program on a computer. FFT program generates a frequency spectrum ready for analysis. In this study, the FTIR process was performed using Thermo-Fisher scientific Nicolet iS10 FTI-R spectrometer.

4.6 Photometry for chloride measurement

Chloride measurement was done using Milwaukee Instruments, MI414 model Chloride professional photometer as shown in Figure 13. To make sure the chloride ppm is within the measurable limits of the photometer the chloride mixed sample was diluted by a factor of hundred using distilled water. Two cuvettes to be used for the experiment were filled with 10 ml of distilled water each. First of the two cuvettes was used as a blank sample while other was used for the sample to be tested for Cl. 0.5 ml reagent-1 (Thiocyanate and Mercury reagent) was added to both cuvettes and was thoroughly swirled for 30 s. Following it, 0.5 ml of reagent-2 (Nitric Acid) was added to both cuvettes and

the cuvettes were swirled for another 30 seconds. Now, the blank sample was placed in the photometer for the first blank measurement after which the photometer was zeroed for calibration purpose. After zeroing, then the liquid sample cuvette was placed in the photometer which displayed the chloride content in the liquid sample in ppm.

Figure 13 Photometer used for Chloride measurement.

Total Chlorine in the sample solid phase was measured using the ASME D-42081 standard. The method comprised of the following steps: firstly, the weighed sample was burned completely in a combustion bomb at oxygen pressure on ~3 MPa. 2% Na_2CO_3 solution was then added to the bomb and reaction was allowed to complete. The bomb was then washed using measured quantity of water. These washings were collected, and their ionic strength was adjusted using $NaNO_3$ solution. Finally, using potentiometric titrator (Metrohm 916 Ti-Touch) total chlorine content of the solid material is determined by measuring the potential of the solution with a chlorine ion-selective electrode with silver nitrate solution.

5 Current results

5.1 Feedstock characterization

Proximate analysis. The feedstock proximate analysis results shown in Table 4 are for the 40% plastic and 60% fiber/paper blend. The values were obtained by averaging results from a minimum of ten different batches of feedstock produced. As mentioned earlier, the values of moisture, ash content, volatile matter, fixed carbon, and calorific value were measured based on ASTM E871, ASTM D1102, ASTM D3175, ASTM D3175 and ASTM E711 respectively.

Table 4 Proximate analysis of CE waste-blend feedstock.

Component	**Values ± SD**
Moisture (%)	3.3 ± 0.5
Ash (%)	6.0 ± 0.6
Volatiles (%)	83.5 ± 2.6
Fixed Carbon (%)	7.2 ± 2.0
HHV, kJ/kg	26.10 ± 1.05

It can be observed from the results that feedstock consists of about 3% moisture and 6% ash showing that the feedstock is very dry and has a low ash content. Also, the high percentage of volatiles make it a good feedstock for pyrolysis process. The HHV is in the range of bituminous coals [86]. The moisture content is also very low as compared to coal [86,87]. The details of the contents of ash are described below separately in Table 5. The ash analysis was done conforming to the ASTM D3682 standard.

Table 5 Characterization of ash.

Ash constituent	**%**
SiO_2	33±18
Al_2O_3	27±11
CaO	21±12
TiO_2	7.2±3.4
MgO	3.0±3.0
Na_2O	1.6±0.7
Fe_2O_3	0.9±0.9
K_2O	0.6±0.4
BaO	0.2±0.2
MnO_2	0.02±0.01
Others	2.8±1.4

It can be noted from Figure 14 that the ash constitutes primarily of silicon dioxide, aluminum oxide, calcium oxide, titanium dioxide and magnesium oxide contributing to total ~90% of the ash.

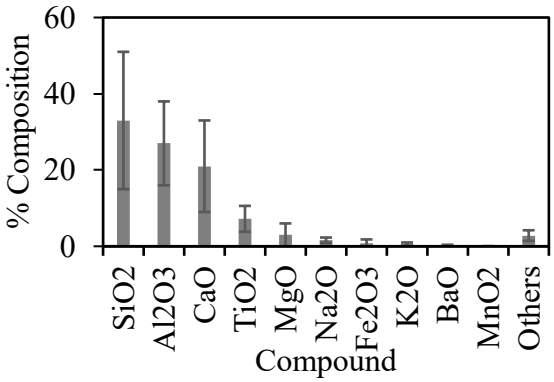

Figure 14 Ash content distribution.

Ultimate analysis. Table 6 shows the results for the ultimate analysis of the 40% plastic and 60% fiber/paper blend. The values were obtained by averaging results from at least ten different batches of feedstock produced. The carbon, hydrogen, and nitrogen percent are based on standard test based on ASTM D5373 method. The oxygen content result is based on ASTM D3176.

Table 6 Ultimate analysis of feedstock.

Component	**Percentage (%)**
Carbon	55.4±1.8
Hydrogen	7.9±0.3
Nitrogen	0.3±0.1
Oxygen	27.1±1.6
Sulfur	0.2±0.1

The blend has low sulfur and nitrogen content which is lower than the powder river basin (PRB) coal [87]. The other elements like Chlorine and Mercury found in the blend are enlisted in Table 7.

Table 7 Other elements found in the feedstock.

Other elements	**ppm ± SD**
Chlorine	1162±487
Fluorine	75±75
Mercury	0.01±0.01
Tin	2.9±0.9

Arsenic	1.1±0.9
Beryllium	0.3±0.8
Chromium	2.2±1.2
Cobalt	0.21±0.16
Lead	1.1±1.4
Nickel	0.81±0.57
Selenium	1.5±1.8

It can be noted that the element of mercury is mostly zero. It is important result, it is a major health and environmental hazard [88] along with other issues described in Table 3. Chlorine amounts found in the feedstock are noticeable and thus feedstock needed treatment. The treatment methods were discussed previously, and the details are discussed in Chlorine removal section.

5.2 Heat transfer analysis

5.2.1 Batch

Pyrolysis experiments for this study were carried out in a batch reactor by introducing feedstock in a container (bomb) placed in convective furnace at 500 ˚C, with the initial temperature of the particle, T_o, at ambient temperature. The material was placed in the container in furnace which was stationary. It is assumed that temperature of the pyrolysis container wall is equal to temperature of furnace after equilibrium was achieved. In this case, the sample was heated by heat transported from the hot walls at temperature (T_w) to the particle surface by convection; the heat was then transported into the particle by conduction.

To determine the regime that best fits the system behavior, we start the analysis with Biot number (Bi) and thermal Thiele modulus (M); the former is related to the heating

regime of the particle, and the latter relates to the propagation of the torrefaction reaction within the particle. The *Bi* and *M*, which are defined as:

$$Bi = \frac{h}{\lambda/L_c} \quad (1)$$

$$M = \frac{R^{\dagger}}{\lambda/(c_p L_c^2)} \quad (2)$$

where h is the convective heat transfer coefficient, λ is the particle thermal conductivity, L_c is the particle characteristic length, $R^{\dagger}$ is the pyrolysis reaction rate within the particle, c_p is the particle heat capacity, and ρ is particle density. The parameters required to determine *Bi* and *M* from equations (1) and (2) are not easy to determine as the material is not well defined (due to mix of several types of fibers/plastic) and therefore, we can only provide an estimate.

The value of heat transfer coefficient, h, was selected to be 10 (W/m^2-K) and was the closest to the flow conditions prevailing in the furnace [89]. The value for thermal conductivity, λ, varies between 0.15 (W/m-K) for PVC, to 0.38 (W/m-K) for polyethylene; for biomass and fibers the values range in 0.03-0.29 (W/m-K) [90]. In this study, the average density was 800 (kg/m^3) for the loose fiber/paper material and 850 (kg/m^3) for the plastic [91]. Heat capacity was taken from the literature to yield an acceptable value of 1400 (J/kg-K) for fiber/paper and ~1400 (ranges from 1300-1670) for plastic. Table 8 summarizes all properties required for the determination of *Bi* and *M*, yielding values for (i) *Bi* of ~0.05 (ii) *M* of ~1.4. The values for *Bi* in the range ~0.1 indicate that the rate of heat transfer by convection from the furnace walls to the particle was lower than the rate of heat transfer into the particle. The value of *M* indicates that the reaction rate was higher

than the heat transfer into the particle. Therefore, this analysis indicates reaction propagation was governed by ***the convection*** from the container walls to the surface of particle, after which the particle temperature equilibrates instantly.

Table 8 Estimated values for the parameters to determine the Bi and M.

Parameter	**Value**
h, W/m^2-K	10
λ for plastic material, W/m-K	0.15-0.38
λ for fiber material, W/m-K	0.03-0.29
R† for fiber and plastic material, kg/m^3-s	600
ρ for fiber material, kg/m^3	800
ρ for plastic material, kg/m^3	850
cp, J/kg-K	1400
Lc thickness, m	0.0005
Bi	0.05
M	~1.4

Establishing that the pyrolysis reaction rate was controlled by the convective heat transfer from the wall to the particle surface and that the particle temperature was uniform always, means that the reaction propagates with the rate of ramp-up of the particle temperature. To calculate the particle temperature, the equation of the heat rate, *dQ(t)/dt*, from the walls to the particle surface was needed to be solved, which was equal to

$$\frac{dQ(t)}{dt} = hA[T_w - T_s(t)] \qquad (3)$$

where T_w and $T_s(t)=T(t)$ are wall and particle surface (or particle) temperatures, respectively. $Q(t)$ is the heat required to increase the particle temperature, or

$$Q(t) = mc_p[T(t) - T_o] + mh_r \qquad (4)$$

where m and c_p are particle mass and specific heat capacity, respectively, T_o is the particle core temperature, which is also equal to the initial temperature of the particle, and h_r is enthalpy of reaction. It was a challenge to find values for h_r as the pyrolyzed material was

not well defined, it comprises fibers (mostly cellulose) and a large variety of plastic materials. Cellulose pyrolysis in the 25-500 ˚C temperature range, starts as an endothermic reaction and continues as an exothermic reaction. Enthalpies of reaction for plastic blends in the same temperature range were always positive and vary in the range (12.55-147.86 J/kg), which is smaller than the value of $c_p(T-T_o)$ in Eq. (4). Thus, for simplification, this term was ignored. Introducing Eq. (4), without h_r, into Eq. (3) and integration from T_w to $T(t)$ yields

$$\frac{T_w - T(t)}{T_w - T_o} = e^{-t/\tau} \qquad (5)$$

where τ is a characteristic time, defined as

$$\tau = \frac{mc_p}{hA} \qquad (6)$$

For the loose material (slab) it is $\tau_{slab}=d\rho c_p/2h$ (d is slab thickness). Rearrangement of Eq. (5) yields

$$T^*(t) = 1 - (1 - \frac{T_o}{T_w})e^{-t/\tau} \qquad (7)$$

T^* is defined as

$$T^*(t) = \frac{T(t)}{T_w} \qquad (8)$$

The required values for determining τ, Eq. (6), for each case are given. Introducing these values in Eq. (6) yields $\tau_{slab}=28$ (s) for fiber and $\tau_{slab}=30$ (s) for plastic, the subscript *slab* is for the loose material. Figure 15 shows the calculation of the temperature from Eq. (8) indicating that the particle reached 400 ˚C (where significant reaction takes place) after 50 (s), which is equivalent to 8 ˚C/s, very close to the value required for fast pyrolysis.

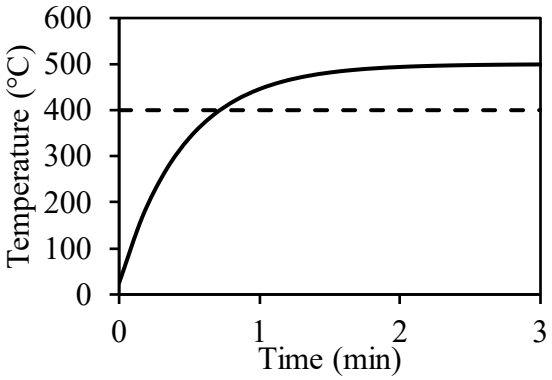

Figure 15 Temperature transients for batch reactor (fiber/plastic material) based on model with characteristic time of ~28 (s).

5.2.2 Continuous paddle

To show that the particles are entrained in the gas flow in our paddle reactor, the experiment was carried out in a paddle reactor. It was found that the suspension of particles depends on two main factors:

A) Size of the particles

B) The rotation speed of the paddles

As seen Figure 16, an experiment with the sawdust/biomass particles of size between 500μm to 3 mm (mostly less than 1 mm) was performed at the rotation frequency of paddles varying from few rpm to 200 rpm. Up to 100 rpm, the particles were mostly creeping on the reactor floor. After exceeding rotation speeds of ~100 rpm, the particles started suspending in the air partially. Finally, at speed of 175 rpm, all the particles were fully suspended. The gas flow fields were clearly seen in the flow of particles.

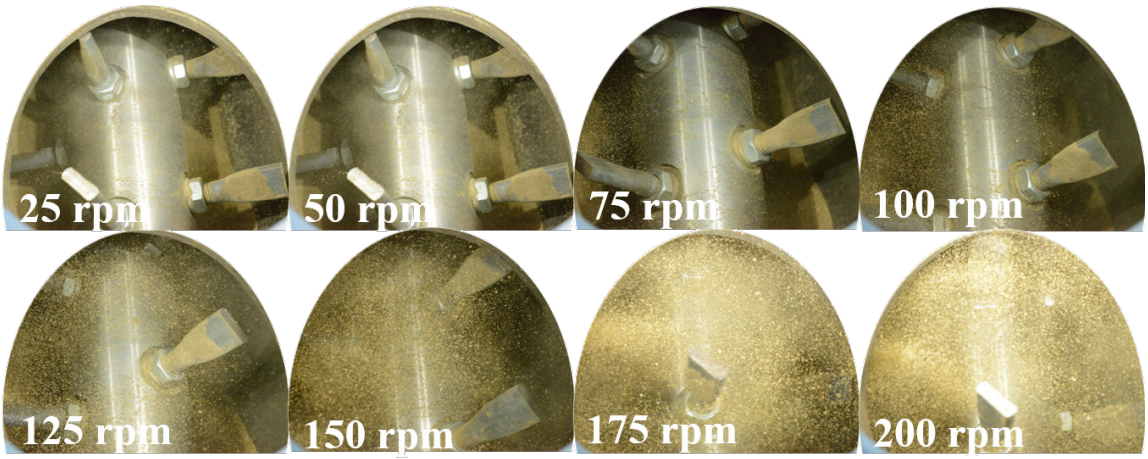

Figure 16 State of particles at various paddle speeds (suspension).

Considering the small size of particles suspended in gas, if we apply properties of fiber and plastic stated in Table 8 to the continuous paddle reactor except that the paddle reactor has a very large convective heat transfer coefficient of at least 250 W/m^2-K [92]. The Bi and M values based on model are ~1 and 0.021, respectively. Based on Biot number value of 1, it can be said that heat transfer rate by conduction is equal to heat transfer by convection. However, as M is equal to 0.021 which is much less than 0.1, the reaction rate is much less than the heat conduction rate. Overall, it can be concluded that reaction propagation rate is governed by convection from walls of reactor to the particles. In this case, the rate at which the particles are reacting depends on the convective heat transfer from the wall to the particle, as concluded also from the batch reactor, thus the same analysis applies here as well, yielding $\tau_{slab}=1.2$ (s). The temperature vs. time curve based on model is shown in Figure 17, indicating that the particle reaches 400 ˚C in < 2 (s), or a heating rate of ~200 ˚C/s.

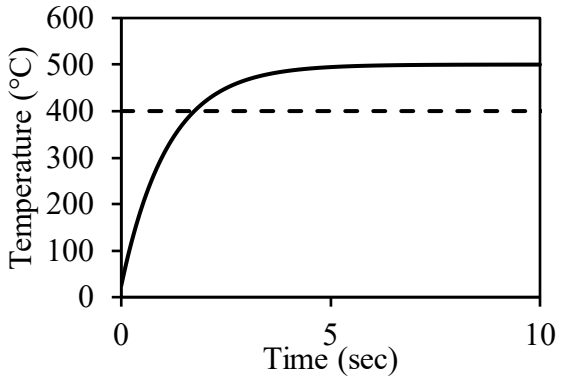

Figure 17 Temperature vs. time plot for continuous paddle reactor based on model.

The above analysis is applicable if the particles were at size in the range 1-3 mm, as can be achieved in biomass grinding. We note that we will flow fiber and plastic flakes that are 10×10 mm, with a thickness of <1 mm into the reactor. We also note that when either fiber and plastic flakes are torrefied they become very brittle as seen by Zhuo et al. [93] and can be grinded rather easily by the paddles that act as blades. Indeed, in the 1-inch reactor (as well as in the batch reactor) the char was in the form of a very fine powder. Although this has not been proven in the 4-inch reactor, it is likely to happen and thus we expect that this this analysis is valid for these feedstocks as well.

5.3 Pyrolysis oil

Pyrolysis oil was produced using the method described in batch pyrolysis section. Table 9 shows pyrolysis results for fiber feedstock. The pyrolysis experiment was at least triplicated, and result for liquid and char yield are shown below. It can be noted that for pyrolysis of fiber/paper, liquid yields were on average 50.3% with standard deviation of 1.0% and char was 26.7%. The total condensable and non-condensable gas yield can be

obtained by subtracting char weight from total feedstock weight. Thus, for fiber pyrolysis, it can be estimated that total condensable + non-condensable gas yield is ~73%.

Table 9 Pyrolysis oil from fiber feedstock.

Exp #	**Weight of feedstock (g)**	**Weight of liquid (g)**	**Liquid yield (%)**	**Weight of char (g)**	**Char (%)**
1	257.2	129.1	50.2	64.5	25.1
2	254.5	130.8	51.4	70.6	27.7
3	259	128	49.4	70.4	27.2
		Average	50.3		26.7
		S. D	1.0		1.4

Similarly, triplicate experiment was performed for the plastic feedstock which yielded average char yields of ~10.3%. Total condensable and non-condensable gas yield obtained by char subtraction from feedstock weight is ~89.7%. This yield from plastic is higher than the fiber yield. Based on few preliminary experiments the liquid yield from plastic pyrolysis was ~65%. The oil obtained from batch pyrolysis is characterized for detailed understanding in the following section.

5.4 Pyrolysis-oil characterization

5.4.1 Fiber

As described earlier in batch system pyrolysis method, the fiber-based bio-oil was obtained from the fiber/paper obtained from CE which consisted of a variety of cardboard and paper. The batch pyrolysis reactor was maintained at 500 °C and transfer lines were maintained at 250 °C to avoid the condensation before the collection system.

Approximately, 250 grams of feedstock was pyrolyzed in each sample. Two fractions separate fractions as seen in Figure 18 were observed. One fraction was water soluble fraction (WS) and was lighter in color while the other fraction was Water Insoluble

fraction (WI) which was more viscous and darker in color. The experiment was triplicated to ensure repeatability of results.

Figure 18 Top fraction (left) and bottom fraction (right) of pyrolysis oil from fiber.

FTIR, HPLC and GC-MS analysis were performed on these samples to understand chemical constituents of the bio-oil. However, as bio-oil is blend of more than 300 compounds and it is difficult to identify all these compounds.

5.4.1.1 FTIR

FTIR spectral analysis was performed for the two different layers of oil separately. It provided information on the chemical functional groups present in the bio-oil fractions. FTIR spectroscopy revealed that the top aqueous layer contained hydroxyl (~3500 cm^{-1}), methylene/methyl (2800-2980 cm^{-1}), carboxylic acid (~1715 cm^{-1}), unconjugated ketone/aldehyde carbonyl (1730-1700 cm^{-1}), and conjugated ketone/aldehyde carbonyl (1700-1675 cm^{-1}) groups [94].

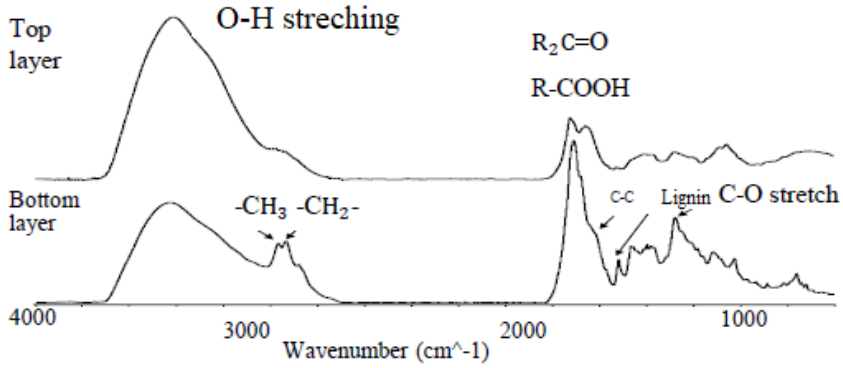

Figure 19 FTIR spectra of pyrolysis bio-oil top and bottom layers.

The bottom organic layer FTIR spectra (refer Figure 19) also showed the same bands as above, but additionally, it also shows bands assigned to lignin (1610, 1517, and 1280 cm^{-1}) and is most likely pyrolytic lignin [95].

5.4.1.2 HPLC

High Performance Liquid Chromatography (HPLC) was performed on bio-oil. Analysis of top layer showed that it contained levoglucosan (3.3%), furfuryl alcohol (6.3%), formic acid (4.3%), acetic acid (3.7%), propionic acid (0.5%), hydroxymethyl-furfural (0.5%), and furfural (0.3%). The GC-MS analysis also confirmed the identity of these compounds. Table 10 shows results from HPLC indicating that 20%±2% of the bio-oil originates from a few groups in cellulose: Levoglucosan, furfuryl alcohol, formic Acid, and acetic acid.

Table 10 Compounds from cellulose.

Compounds in bio-oil	ug/mg	
	Ave	**SD**
Glucose	0.3	0.1
Xylose	3.0	0.7
Levoglucosan	33.2	2.8
Furfuryl alcohol	63.3	3.1
Formic Acid	42.7	13

Acetic acid	37.2	2.1
Propionic Acid	6.9	1.2
Hydroxy-methyl-furfural	4.8	0.5
Furfural	2.7	0.3
Total	194	23

5.4.1.3 GC-MS

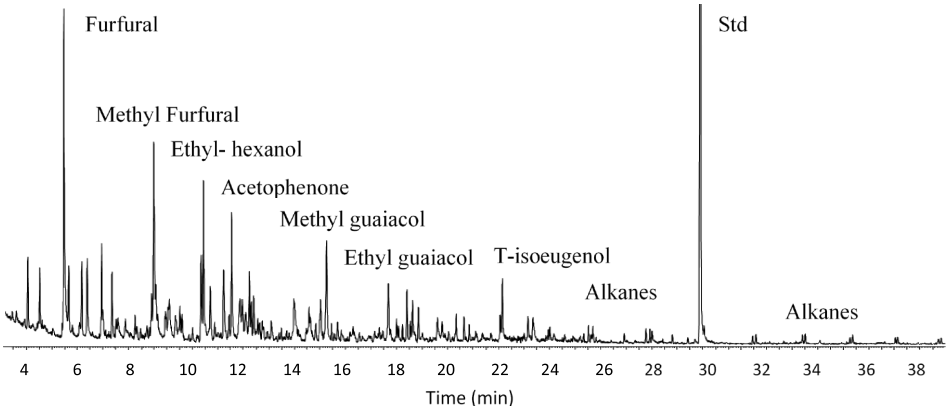

Figure 20 GC-MS analysis of fiber/paper pyrolysis oil from bottom layer.

GC-MS was used to analyze the volatile components in the bio-oil bottom layer. This fraction contained mainly lignin derivatives (55%) with the major compounds being methyl-phenol, methyl styrene, acetophenone, guaiacol, methyl-guaiacol, ethyl guaiacol, and isoeugenol. This mixture is consistent with woody biomass pyrolysis products. Alkanes (C_{10}-C_{21}) and volatile carbohydrate derivatives (28%) were also detected. The alkanes are likely to originate from polyethylene or wax.

GC-MS analysis not only confirmed the identity of the compounds found in the top layer by HPLC but also showed several carbohydrate degradation products (3-methyl-1,2-cyclopentanedione, dianhydro-hexoses, 2,3-dimethyl-2-cyclopenten-1-one, 2-methyl-2-cyclopentenone, and methyl-guaiacol).

5.4.1.4 ESI-MS

The limitation of GC-MS results is that only volatile and semi volatile compounds can be analyzed, which accounts for only a portion of the bio-oil. ESI-MS is successfully used to characterize pyrolysis bio-oil [96] to obtain the average molar mass (M_n and M_w) of bio-oil samples.

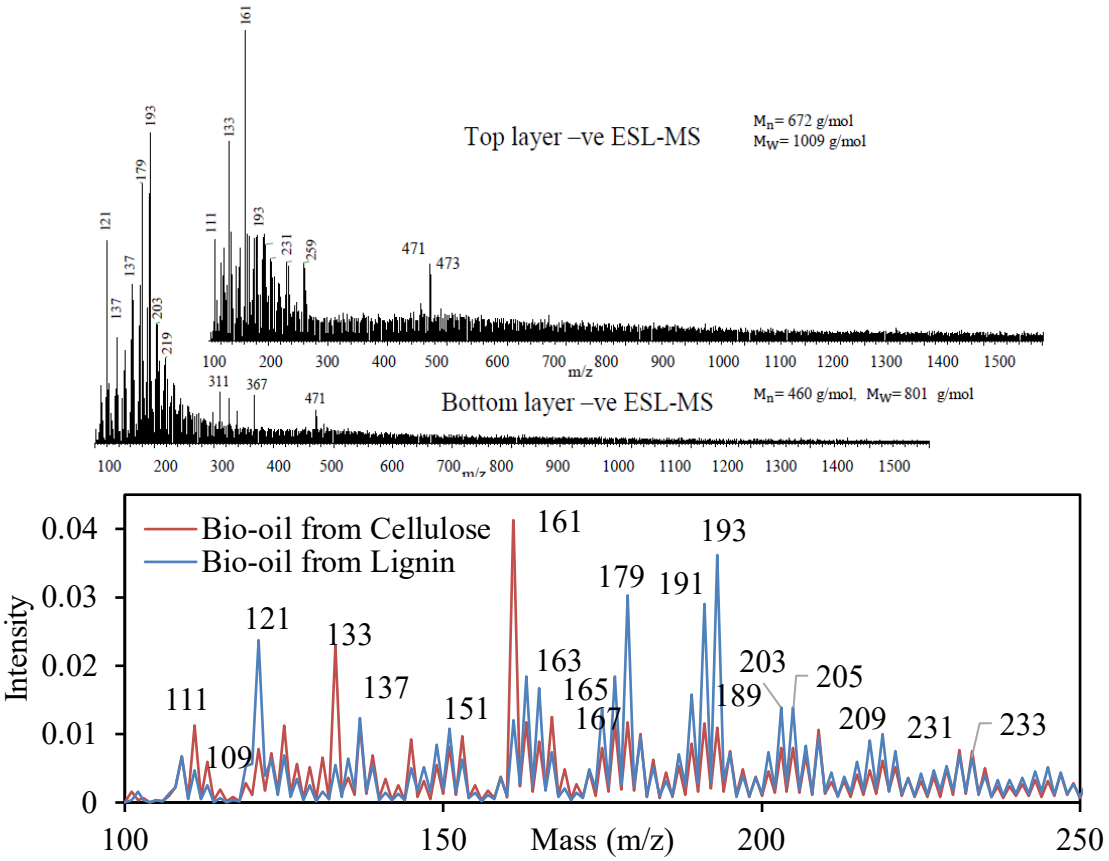

Figure 21 Negative ion ESI-MS of bio-oil top layer (cellulose) and bottom layer (lignin) showing mass spectrum **(Top)** in m/z= 100 to m/z=1500 range. **(Bottom)** overlap in m/z= 100 to m/z=250 range.

The M_w and M_n of the bio-oil top layer was determined by negative ion ESI-MS (refer Figure 21). The M_w was 1009 g/mol and M_n was 672 g/mol. These results clearly show that the products were mono- to oligomeric compounds. The major peaks observed

in the negative ion spectrum ([M-H]-) include m/z at 161 ($C_6H_{10}O_5$, levoglucosan), 125 ($C_6H_6O_3$, hydroxy-methyl-furfural), and 143 ($C_6H_8O_4$, dianhydro-hexosan), which supports the HPLC findings.

Negative ion ESI-MS of the bio-oil bottom layer was also employed and gave M_w and M_n values of 801 and 460 g/mol. Again, this shows that the bottom bio-oil layer contains a range of oligomeric products. The major peaks observed in the negative ion spectrum ([M-H]-) include m/z at 109, 137, 151, 163, 179, and 193 were tentatively assigned to benzenediol (or methylfurfural), methyl-guaiacol, ethyl-guaiacol, isoeugenol, coniferyl-alcohol, and propenyl-syringol, respectively and support the GC-MS findings. These results are also consistent with literature [97,98].

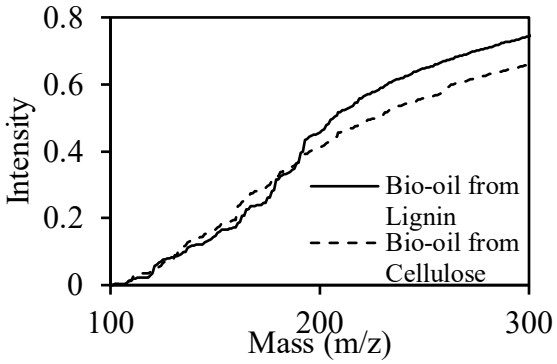

Figure 22 Cumulative mass (m/z) from range of 100 to 300 showing inversion of lignin and cellulose production trend after m/z of 180.

Figure 22 show the accumulative mass intensities (m/z) for cellulose and lignin layers. It can be noted that in range of 150 to 180 the amount of cellulose produced is much more than the amount of lignin. However, the trend completely reverses in the range of 180-300, where the amount of lignin produced is much higher than the amount of cellulose produced.

5.4.2 Plastic

5.4.2.1 GC-MS

GC-MS analysis for the plastic samples obtained from the CE plastic blends is shown in Figure 23. Triplication was done to ensure repeatability of results. 85 peaks were detected in the sample. Trichlorobenzene (14.19 m/z) was used as internal standard. To find the similarity between the plastic derived oil and the diesel fuel used in industry the GC-MS results of standard diesel analysis (refer Figure 24) were compared with the plastic derived bio-oil. The comparison Figure 25 clearly showed that ~ 60% to 65% of the plastic derived bio-oil composition is similar to that of diesel fuel with most matching compounds seen in C8 to C24 region.

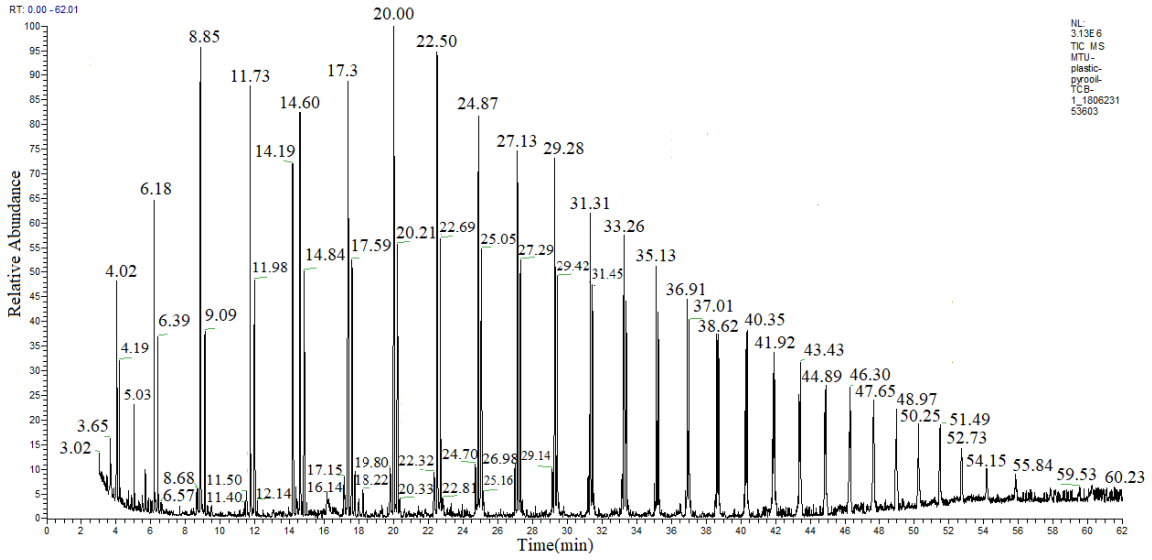

Figure 23 GC-MS (TIC) of bio-oil from plastic feedstock.

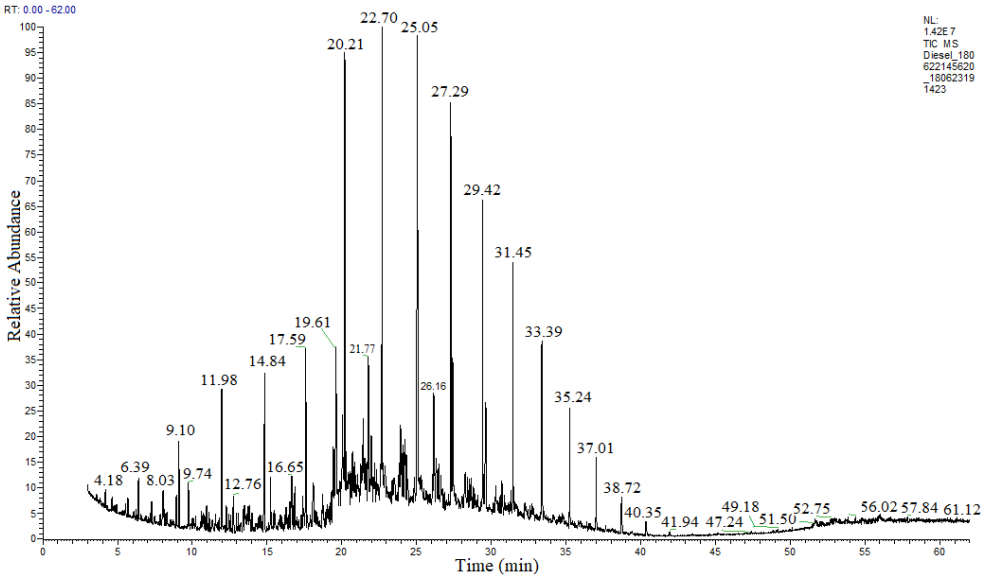

Figure 24 GC-MS (TIC) of diesel sample.

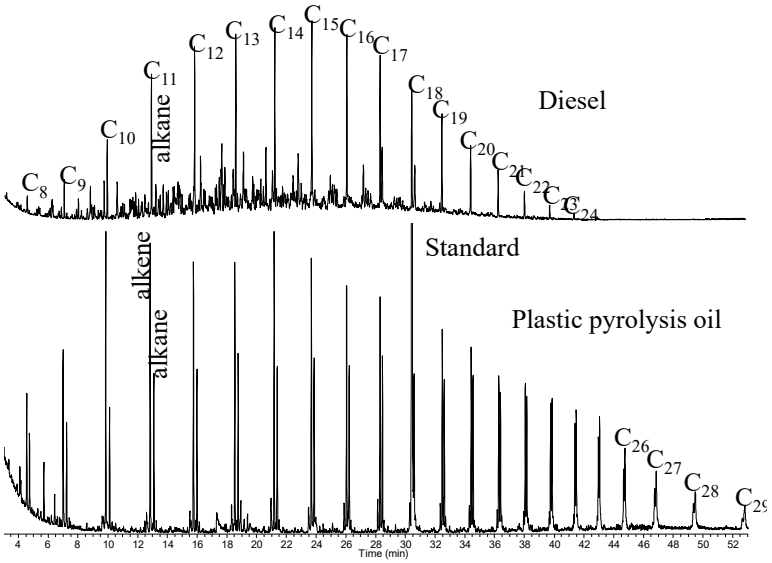

Figure 25 Comparison of GC-MS of plastic oil and diesel.

5.4.2.2 Chlorine removal

The chlorine removal was done by doing torrefaction at 300 °C followed by a high shear mixing as described in chlorine removal section. Figure 26 (left) shows results for the mass loss of plastic in the torrefaction. Figure 26 (right) shows the high shear mixing times vs. chloride removed from original sample in ppm. Although there are differences

between two transients the trends are similar and within the experimental error. The results clearly show that high shear method clearly removed chlorine from the torrefied sample. It should be noted that attempts to remove chlorine by high shear mixer for un-torrefied plastic failed as the material did not grind.

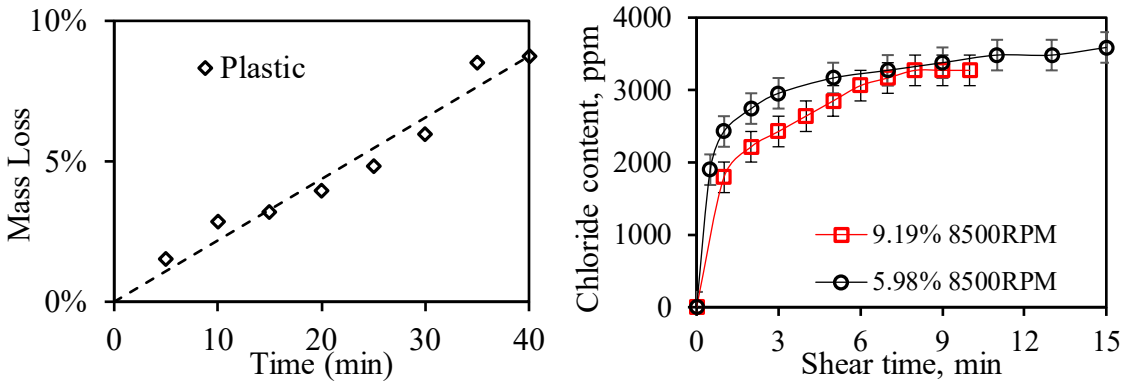

Figure 26 (Left) Mass loss for plastic during torrefaction at 300°C (Right) Chlorine removal vs. high shear mixing time.

5.4.3 Fiber-plastic blend

5.4.3.1 FTIR

The CE waste mix plus fiber (20 random pieces selected) was analyzed by FTIR spectroscopy to determine their chemical identity with spectra library matching. The mix was shown to be comprised of three cellulose/paper, three polypropylene (PP), three polyethylene (PE), four polyethylene terephthalate (PET), silicone, three cellulose/silicone mix, two paper/acrylate mix and one nylon samples. A composite FTIR spectrum is shown Figure 27 shows the major bands associated with PE, PP, PET, and paper. No characteristic bands at 610 cm^{-1} (C-Cl stretch) and 1425 cm^{-1} (C-H_2 bending) were observed for polyvinylchloride.

All the samples had C-H stretching bands at assigned to methyl (2960 cm^{-1} and 2870 cm^{-1}) and methylene (2916 cm^{-1} and 2850 cm^{-1}) groups mainly associated with PP and PE plastic. The O-H stretching band 3100-3600 cm^{-1} was present in all samples and progressively decreased in intensity upon the extent of torrefaction due to dehydration reactions. A broad carbonyl (C=O) band at 1690-1750 cm^{-1} was observed and assigned to mainly an ester in linkage in PET and acrylate and an amide linkage in nylon. A small band at 1505 cm^{-1} was assigned to lignin from paper. The spectral region between 1000 and 1070 cm^{-1} has been assigned to C–O stretching in wood cellulose and hemicellulose and decreased in intensity with torrefaction mass loss. All samples were shown to have cis- and trans-vinylene bands at 727 cm^{-1} and 974 cm^{-1}, respectively.

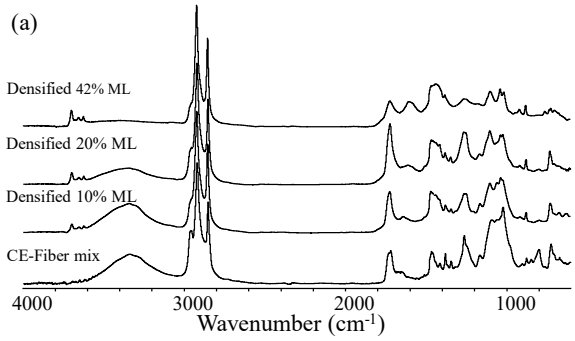

Figure 27 FTIR spectra of CE-fiber mix and ground/screened (425-850 µm) torrefied (10, 20 and 42% mass loss) densified material.

5.4.3.2 Chlorine content

First step in chlorine removal was torrefaction at 300 °C. The torrefaction result of plastic-fiber waste blend is shown in Figure 28 (left). Mass loss starts around 3 minutes and approaches 50% after 30 minutes. After torrefaction, mass loss vs. time curve shows the torrefaction behavior. High shear experiments of torrefied material followed the torrefaction for chlorine removal and aqueous extracts were obtained, which were filtered

and measured for chloride in the solution and chlorine in the solid powder. Figure 28 (Right) shows chloride in solid filtrate after high shear and chlorine in aqueous solution.

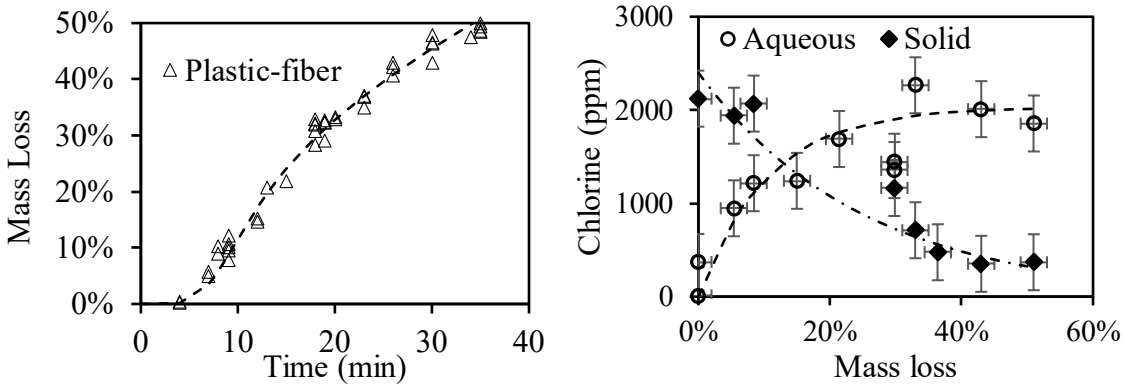

Figure 28 (left) Mass loss vs. time (right) chloride in solid filtrate after high shear and chlorine in aqueous solution.

There was a large scatter in the experiments originating from the fact that in these experiments, the samples were small (2-3 grams) and the composition may differ significantly in its content and may not well represent the actual case. Nevertheless, there was a clear trend: (i) in the aqueous solution there was little-to-no chloride at zero mass loss (no torrefaction); (ii) the chloride in the aqueous solution increases gradually until ~25% mass loss, after which it stays constant at an asymptotic value of 2043±207 ppm; (iii) chlorine in the solid phase has a value of 2031±129 at zero mass loss, then decreases gradually to ~10% of the initial value.

6 Future work

Heat transfer model for fast-pyrolysis in batch reactor was provided, demonstrating that it can be used for fast pyrolysis experiments and the results are comparable to continuous reactor can be achieved. The effectiveness of chlorine removal method using torrefaction and high shear mixing was proven. For characterization of pyrolysis oil produced in batch reactor, analytical methods of GC-MS, FTIR, ESI-MS and HPLC were used to identify the constituent compounds. It was found that pyrolysis oil produced from fiber/paper has two different fractions with top fraction consisting mostly cellulose and bottom fraction consisting lignin. Based on FTIR, common bands in both layer like hydroxyl, methylene/methyl, carboxylic acid, unconjugated and conjugated ketone/aldehyde carbonyl groups were identified with exception of lignin related compound band which was observed only for bottom layer. Also, other common compounds like levoglucosan, furfuryl alcohol, formic acid, acetic acid, propionic acid, hydroxymethyl-furfural, and furfural, levoglucosan, hydroxy-methyl-furfural, etc. were identified and verified using the other mentioned analytical methods. For pyrolysis oil produced from fast pyrolysis of plastic, it was found that it had 60-65% compounds like the diesel fuel.

This following paragraph restates the general objectives presented in Section 2. The final goal of this workplan is investigating the synergistic effect in co-pyrolysis of fiber plastic feedstock. The broader plan involves study of fiber and plastic feedstock individually followed by a study of fiber-plastic blend. The key steps involved in fulfilling

these objectives are elaborated below with respect to the key parameters needed for achieving these individual objectives:

Objective 1: Investigate kinetics and product distribution in fast pyrolysis of fiber and plastics.

1. ***kinetics:***

To study the kinetics, two different reactors will be used: batch fast pyrolysis reactor and continuous paddle reactor. The focus for this work will be on the batch fast pyrolysis reactor. The experiments in this type of reactor will use an improved batch pyrolysis reactor. This improved reactor will consist of two key types of apparatuses: (1) fast pyrolysis apparatus (2) measurement apparatus

The fast pyrolysis apparatus will consist of a setup with following key components (a) pyrolysis container (bomb), (b) heaters for heating the container, (c) high speed mixing mechanism (d) condensation and oil collection unit, and (e) bubbling mechanism (scrubbing) for release of incondensable gases. The measurement apparatus will include the following key components: (a) thermocouple for temperature measurement inside the batch pyrolysis container, (b) pressure sensor following the oil collection system and (c) gas analyzer to measure non-condensable gases like CO and CO_2.

To investigate the kinetics in the fast pyrolysis process in improved batch pyrolysis reactor experiments for the measurement of pyrolysis temperature, heat transfer rate and reaction rates will be designed. The experiments will have a similar setup as shown in Figure 3 with an addition of mixing mechanism in the pyrolysis container (bomb), a purge

gas mechanism and various sensors as listed above. The basic design for the experiment is described in the following paragraphs.

The key parameters which will be focused on are (a) heat transfer rate, (b) pyrolysis temperature, (c) reaction rate, and (d) vapor residence time. The heating rate ensures if the process is fast pyrolysis process. The rotation speed of the mixing blade will primarily govern this rate as higher mixing speeds increase the heat transfer rates. The increased heat transfer rates will decrease the time needed for the start of reaction as well as completion of reaction. The time at which reaction starts and ends can be distinguished with its effect on pressure. Thus, the pressure transient from the sensor located after the condensation system will be important indicator of the times. As seen in Figure 29 it is anticipated that the pressure change will follow a Gaussian distribution with width of distribution showing the times required for the reaction. With the increase in rotation speed of the mixer the heat transfer rates would increase, and this will be reflected in the shrinking of the distribution along with curve shifting to left as seen in Figure 29. With start and end times of the reaction the reaction rates can be calculated. This will also help in studying the effect of mixing speed which is an important operational parameter for the batch as well as the continuous paddle reactor.

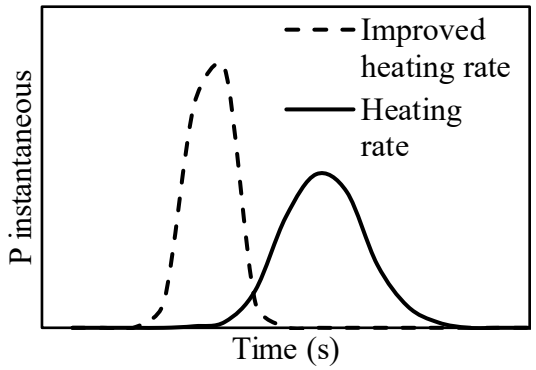

Figure 29 Effect of heating rate in P instantaneous vs time plot.

The next parameter that will be investigated is the temperature of the pyrolysis. The temperature inside the batch reactor will be set using the controller and the temperature will be measured using a thermocouple inside the pyrolysis container (reactor bomb). The temperature transient will enable the study of effect of temperature on the kinetics.

The other parameter that will be studied is residence time of the pyrolytic vapors formed after the reaction. It is important to have small residence times to avoid the secondary reactions of the vapors. The vapor residence time in this improved batch reactor will be controlled using a flow of a non-reacting purge gas like nitrogen or carbon dioxide. With the increase of purge gas flow rate, the residence time of pyrolytic vapors can be reduced. The mass flow rate can be measured using flow-meter or calculated based on time required for purge gas to pass through the length of reactor.

2. ***for product distribution:***

Fast pyrolysis produces mainly liquid, solids (char) and non-condensable gas yields. To understand the product distribution quantification of liquid, solid and gaseous yields will be done as follow: (a) the liquid yield will be measure by using weight difference

of liquid collection bottle before and after the experiment (b) water percent in the oil will also be measured potentially using a Karl Fisher method (c) the solid yield will be measured by measuring the solid reminder in the container after every experiment (d) the percentage of the incondensable gases will be measured and then analyzed using a gas analyzer for the detailed product formation.

After measurement of product distribution, the liquid fractions (pyrolysis oil) will be analyzed in detail for identification of major compounds and chemical functional groups present in the pyrolysis oil using GC-MS, ESI-MS, FTIR and HPLC. Additionally, a well-studied biomass like Poplar or Arundo Donax will be pyrolyzed in the batch reactor to establish a benchmark for properties.

Objective 2: Investigate the effect of chlorine and other minerals in fast pyrolysis of fiber and plastic. To investigate the effect of fiber and chlorine the pyrolysis experiments will be done using two different feedstocks: (a) untreated feedstock (containing chlorine and minerals) and (b) chlorine free feedstock. Initially, minerals and ash analysis will be performed on feedstock (K, Cl, Na, Ca, Mg, Fe and Al) before the chlorine removal. The chlorine would be removed using the removal method described in section 3.2.3. Untreated feedstock would be initially characterized followed by characterization of pyrolysis oil produced from it. All the tests described in product distribution section will be conducted. For the treated feedstock the chlorine removal parameters like torrefaction temperature and high shear mixing speeds will be investigated using the combination of various temperature and shear mixing speeds. Also, the use of a base solution like NaOH will be implemented

to study the effect. Selective feedstock with best chlorine and mineral removal results will be further used for the pyrolysis procedure.

Objective 3: Investigate the synergistic effects in fast co-pyrolysis of fiber-plastic blends: (a) with/without chlorine and minerals (b) at various fractions of fiber/plastic in the blend, in the range 0.1-0.9. As described in objective 2, two type of fiber-plastic blends will be used (a) with chlorine and minerals (b) without chlorine and minerals. The synergistic effect of co-pyrolysis in the batch reactor will be investigated for above mentioned materials using the parameters as follows: (a) CO_2 an CO gas measurements: Change in the yields of gases like CO_2 an CO can be good indicators of the synergy. Thus, gas analyzer would be used to quantify these gases for on-line understanding of the synergy. (b) operational parameters: Operational parameters of the pyrolysis reactor like temperature of heater, residence time based on purge gas flow rate will be varied and their effect on the yields as well as composition of the product from synergistic point will be investigated. (c) heating rates: Heating rate is based on rotation speed of mixing mechanism in the improved batch reactor. The effect of rotation speed of mixing mechanism (heating rate) will be investigated on synergy.

The product parameters that will be measured to study the synergistic effect will include but not limited to liquid yields, pyrolysis char yields, water content in liquid, gas yield, H/C ratio in liquid yield, oxygen content, average molecular weight in liquid yields, aromatic molecules, viscosity, heating values and acidity. The major compounds that will characterized for liquid oils will be levoglucosan, saccharides, acetic acid, lactic acid, epoxide, alcohols, ethers, phenols, furans, ketones, esters.

Additionally, to compare these results with a well-studied feedstock, biomass like poplar or Arundo Donax will potentially be used as a co-pyrolysis feedstock in the batch reactor to establish a benchmark for above stated properties.

7 Reference List

[1] P. Roy, G. Dias, Prospects for pyrolysis technologies in the bioenergy sector: A review, Renew. Sustain. Energy Rev. 77 (2017) 59–69. doi:10.1016/j.rser.2017.03.136.

[2] T. Bridgwater, Biomass for energy, J. Sci. Food Agric. 86 (2006) 1755–1768. doi:10.1002/jsfa.2605.

[3] A.T. Sipra, N. Gao, H. Sarwar, Municipal solid waste (MSW) pyrolysis for bio-fuel production: A review of effects of MSW components and catalysts, Fuel Process. Technol. 175 (2018) 131–147. doi:10.1016/j.fuproc.2018.02.012.

[4] M.S. Safdari, M. Rahmati, E. Amini, J.E. Howarth, J.P. Berryhill, M. Dietenberger, D.R. Weise, T.H. Fletcher, Characterization of pyrolysis products from fast pyrolysis of live and dead vegetation native to the Southern United States, Fuel. 229 (2018) 151–166. doi:10.1016/j.fuel.2018.04.166.

[5] D. Czajczyńska, T. Nannou, L. Anguilano, R. Krzyzyńska, H. Ghazal, N. Spencer, H. Jouhara, Potentials of pyrolysis processes in the waste management sector, Energy Procedia. 123 (2017) 387–394. doi:10.1016/j.egypro.2017.07.275.

[6] U.S.D. of Energy, 2016 Billion-Ton Report: Advancing Domestic Resources for a Thriving Bioeconomy, 2016. doi:ORNL/TM-2016/160.

[7] I. Burke, L. Lave, Renewable Fuel Standard: Potential Economic and Environmental Effects of U.S. Biofuel Policy, National Academies Press, Washington DC, 2011. doi:10.17226/13105.

[8] Y.N. Lee, The world is scrambling now that China is refusing to be a trash dumping ground, CNBS. (2018). www.cnbc.com/2018/04/16/climate-change-china-bans-import-of-foreign-waste-to-stop-pollution.html.

[9] D. Shane, China refuses to recycle more of the world's trash, CNN. (2018). http://money.cnn.com/2018/04/20/news/economy/china-new-recycling-ban/index.html.

[10] C. Hazen, Paper recovery and Landfill, Recycl. Pap. (2018). http://www.paperrecycles.org/statistics/paper-recovery-landfill. (accessed September 7, 2018).

[11] B.M.H.J. Langholtz, L.M. Stokes, Eaton, 2016 BILLION-TON REPORT Advancing Domestic Resources for a Thriving Bioeconomy, Oak Ridge Natl. Lab. (2016). doi:ORNL/TM-2016/160.

[12] R.J. Evans, T.A. Milne, Molecular characterization of the pyrolysis of biomass, Energy & Fuels. 1 (1987) 123–137. doi:10.1021/ef00002a001.

[13] A. Oasmaa, Y. Solantausta, V. Arpiainen, E. Kuoppala, K. Sipilä, Fast pyrolysis bio-oils from wood and agricultural residues, Energy and Fuels. 24 (2010) 1380–1388. doi:10.1021/ef901107f.

[14] A. V. Bridgwater, Review of fast pyrolysis of biomass and product upgrading, Biomass and Bioenergy. 38 (2012) 68–94. doi:10.1016/j.biombioe.2011.01.048.

[15] U.S.D. of Energy, US Billion-ton update. Biomass Supply for a Bioenergy and Bioproducts Industry, 2011. doi:10.1089/ind.2011.7.375.

[16] T. Werpy, G. Petersen, Top Value Added Chemicals from Biomass Volume I — Results of Screening for Potential Candidates from Sugars and Synthesis Gas Top Value Added Chemicals From Biomass Volume I: Results of Screening for Potential Candidates, 2004. doi:10.2172/15008859.
[17] A.J. Ragauskas, C.K. Williams, B.H. Davison, G. Britovsek, J. Cairney, C.A. Eckert, W.J. Frederick Jr., J.P. Hallett, D.J. Leak, C.L. Liotta, J.R. Mielenz, R. Murphy, R. Templer, T. Tschaplinski, The Path Forward for Biofuels and Biomaterials\r10.1126/science.1114736, Science (80-.). 311 (2006) 484–489. doi:10.1126/science.1114736.
[18] D.M. Alonso, S.G. Wettstein, M.A. Mellmer, E.I. Gurbuz, J.A. Dumesic, Integrated conversion of hemicellulose and cellulose from lignocellulosic biomass, Energy Environ. Sci. 6 (2013) 76–80. doi:10.1039/c2ee23617f.
[19] S.K. Tanneru, D.R. Parapati, P.H. Steele, Pretreatment of bio-oil followed by upgrading via esterification to boiler fuel, Energy. 73 (2014) 214–220. doi:10.1016/j.energy.2014.06.039.
[20] A. V. Bridgwater, D. Meier, D. Radlein, An overview of fast pyrolysis of biomass, Org. Geochem. 30 (1999) 1479–1493. doi:10.1016/S0146-6380(99)00120-5.
[21] D.A. Bulushev, J.R.H. Ross, Catalysis for conversion of biomass to fuels via pyrolysis and gasification: A review, Catal. Today. 171 (2011) 1–13. doi:10.1016/j.cattod.2011.02.005.
[22] G. Lyu, S. Wu, H. Zhang, Estimation and Comparison of Bio-Oil Components from Different Pyrolysis Conditions, Front. Energy Res. 3 (2015) 1–11. doi:10.3389/fenrg.2015.00028.
[23] P.A. Johnston, Thermochemical methylation of lignin to produce high value aromatic compounds, Iowa State University, 2017. doi:http://lib.dr.iastate.edu/etd/15544.
[24] C. Li, J.E. Aston, J.A. Lacey, V.S. Thompson, D.N. Thompson, Impact of feedstock quality and variation on biochemical and thermochemical conversion, Renew. Sustain. Energy Rev. 65 (2016) 525–536. doi:10.1016/j.rser.2016.06.063.
[25] D. Mohan, C.U. Pittman, P.H. Steele, Pyrolysis of wood/biomass for bio-oil: A critical review, Energy and Fuels. 20 (2006) 848–889. doi:10.1021/ef0502397.
[26] C. Branca, P. Giudicianni, C. Di Blasi, GC/MS characterization of liquids generated from low-temperature pyrolysis of wood, Ind. Eng. Chem. Res. 42 (2003) 3190–3202. doi:10.1021/ie030066d.
[27] B. Klemetsrud, S. Ukaew, V.S. Thompson, D.N. Thompson, J. Klinger, L. Li, D. Eatherton, P. Puengprasert, D. Shonnard, Characterization of Products from Fast Micropyrolysis of Municipal Solid Waste Biomass, ACS Sustain. Chem. Eng. 4 (2016) 5415–5423. doi:10.1021/acssuschemeng.6b00610.
[28] H. Hassan, J.K. Lim, B.H. Hameed, Recent progress on biomass co-pyrolysis conversion into high-quality bio-oil, Bioresour. Technol. 221 (2016) 645–655. doi:10.1016/j.biortech.2016.09.026.
[29] E. Alsbou, B. Helleur, Direct infusion mass spectrometric analysis of bio-oil using ESI-Ion-trap MS, Energy and Fuels. 28 (2014) 578–590. doi:10.1021/ef4018288.
[30] M. He, B.U. Cho, J.M. Won, Effect of precipitated calcium carbonate - Cellulose

nanofibrils composite filler on paper properties, Carbohydr. Polym. 136 (2016) 820–825. doi:10.1016/j.carbpol.2015.09.069.
[31] Y. Zheng, L. Tao, X. Yang, Y. Huang, C. Liu, Z. Zheng, Study of the thermal behavior, kinetics, and product characterization of biomass and low-density polyethylene co-pyrolysis by thermogravimetric analysis and pyrolysis-GC/MS, J. Anal. Appl. Pyrolysis. 133 (2018) 185–197. doi:10.1016/j.jaap.2018.04.001.
[32] V.I. Sharypov, N. Marin, N.G. Beregovtsova, S. V. Baryshnikov, B.N. Kuznetsov, V.L. Cebolla, J. V. Weber, Co-pyrolysis of wood biomass and synthetic polymer mixtures. Part I: Influence of experimental conditions on the evolution of solids, liquids and gases, J. Anal. Appl. Pyrolysis. 64 (2002) 15–28. doi:10.1016/S0165-2370(01)00167-X.
[33] D.K. Ojha, R. Vinu, Fast co-pyrolysis of cellulose and polypropylene using Py-GC/MS and Py-FT-IR, RSC Adv. 5 (2015) 66861–66870. doi:10.1039/c5ra10820a.
[34] H. Yuan, H. Fan, R. Shan, M. He, J. Gu, Y. Chen, Study of synergistic effects during co-pyrolysis of cellulose and high-density polyethylene at various ratios, Energy Convers. Manag. 157 (2018) 517–526. doi:10.1016/j.enconman.2017.12.038.
[35] S.D. Gunasee, B. Danon, J.F. Görgens, R. Mohee, Co-pyrolysis of LDPE and cellulose: Synergies during devolatilization and condensation, J. Anal. Appl. Pyrolysis. 126 (2017) 307–314. doi:10.1016/j.jaap.2017.05.016.
[36] G. WANG, A. LI, Thermal Decomposition and Kinetics of Mixtures of Polylactic Acid and Biomass during Copyrolysis, Chinese J. Chem. Eng. 16 (2008) 929–933. doi:10.1016/S1004-9541(09)60018-5.
[37] M. Brebu, S. Ucar, C. Vasile, J. Yanik, Co-pyrolysis of pine cone with synthetic polymers, Fuel. 89 (2010) 1911–1918. doi:10.1016/j.fuel.2010.01.029.
[38] Y. Xue, Thermochemical conversion of organic and plastic waste materials through pyrolysis, Iowa State University, 2017. http://lib/dr.iastate.edu/etd/16242.
[39] E. Önal, B.B. Uzun, A.E. Pütün, Bio-oil production via co-pyrolysis of almond shell as biomass and high density polyethylene, Energy Convers. Manag. 78 (2014) 704–710. doi:10.1016/j.enconman.2013.11.022.
[40] W. Chen, S. Shi, J. Zhang, M. Chen, X. Zhou, Co-pyrolysis of waste newspaper with high-density polyethylene: Synergistic effect and oil characterization, Energy Convers. Manag. 112 (2016) 41–48. doi:10.1016/j.enconman.2016.01.005.
[41] J.D. Martínez, A. Veses, A.M. Mastral, R. Murillo, M. V. Navarro, N. Puy, A. Artigues, J. Bartrolí, T. García, Co-pyrolysis of biomass with waste tyres: Upgrading of liquid bio-fuel, Fuel Process. Technol. 119 (2014) 263–271. doi:10.1016/j.fuproc.2013.11.015.
[42] P.T. Williams, R. Bagri, Hydrocarbon gases and soils from the recycling of polystyrene waste by catalytic pyrolysis, Int. J. Energy Res. 28 (2004) 31–44. doi:10.1002/er.949.
[43] Q. Meng, X. Chen, C. Bu, J. Ma, Controlled air oxidation of plastic and biomass in a packed-bed reactor, Chem. Eng. Technol. 37 (2014) 43–48. doi:10.1002/ceat.201300310.
[44] Y. Xue, Thermochemical conversion of organic and plastic waste materials through pyrolysis, 2017. https://lib.dr.iastate/etd/16242.

[45] L. Chen, S. Wang, H. Meng, Z. Wu, J. Zhao, Study on Gas Products Distributions during Fast Co-pyrolysis of Paulownia Wood and PET at High Temperature, Energy Procedia. 105 (2017) 391–397. doi:10.1016/j.egypro.2017.03.331.
[46] K.G. Burra, A.K. Gupta, Kinetics of synergistic effects in co-pyrolysis of biomass with plastic wastes, Appl. Energy. 220 (2018) 408–418. doi:10.1016/j.apenergy.2018.03.117.
[47] J. Chattopadhyay, C. Kim, R. Kim, D. Pak, Thermogravimetric characteristics and kinetic study of biomass co-pyrolysis with plastics, Korean J. Chem. Eng. 25 (2008) 1047–1053. doi:10.1007/s11814-008-0171-6.
[48] Ö. Čepelioɬullar, A.E. Pütün, Products characterization study of a slow pyrolysis of biomass-plastic mixtures in a fixed-bed reactor, J. Anal. Appl. Pyrolysis. 110 (2014) 363–374. doi:10.1016/j.jaap.2014.10.002.
[49] Y. Xue, S. Zhou, R.C. Brown, A. Kelkar, X. Bai, Fast pyrolysis of biomass and waste plastic in a fluidized bed reactor, Fuel. 156 (2015) 40–46. doi:10.1016/j.fuel.2015.04.033.
[50] J. Yang, J. Rizkiana, W.B. Widayatno, S. Karnjanakom, M. Kaewpanha, X. Hao, A. Abudula, G. Guan, Fast co-pyrolysis of low density polyethylene and biomass residue for oil production, Energy Convers. Manag. 120 (2016) 422–429. doi:10.1016/j.enconman.2016.05.008.
[51] K.H. Ko, A. Rawal, V. Sahajwalla, Analysis of thermal degradation kinetics and carbon structure changes of co-pyrolysis between macadamia nut shell and PET using thermogravimetric analysis and 13C solid state nuclear magnetic resonance, Energy Convers. Manag. 86 (2014) 154–164. doi:10.1016/j.enconman.2014.04.060.
[52] M. Sanchez, A. Moran, S. Escapa, L. Calvo, O. Martinez, Simultaneous thermogravimetric and mass spectrometric analysis of the pyrolysis of municipal solid waste and polyethylene terephthalate, J. Therm. Anal. Calorim. 90 (2007) 209–215.
[53] S. Zinchik, J.L. Klinger, T.L. Westover, Y. Donepudi, S. Hernandez, J.D. Naber, E. Bar-Ziv, Evaluation of fast pyrolysis feedstock conversion with a mixing paddle reactor, Fuel Process. Technol. 171 (2018) 124–132. doi:10.1016/j.fuproc.2017.11.012.
[54] M.K. Bahng, C. Mukarakate, D.J. Robichaud, M.R. Nimlos, Current technologies for analysis of biomass thermochemical processing: A review, Anal. Chim. Acta. 651 (2009) 117–138. doi:10.1016/j.aca.2009.08.016.
[55] A. Funke, E. Henrich, N. Dahmen, J. Sauer, Dimensional Analysis of Auger-Type Fast Pyrolysis Reactors, Energy Technol. 5 (2017) 119–129. doi:10.1002/ente.201600095.
[56] A. Hassanpour, H. Tan, A. Bayly, P. Gopalkrishnan, B. Ng, M. Ghadiri, Analysis of particle motion in a paddle mixer using Discrete Element Method (DEM), Powder Technol. 206 (2011) 189–194. doi:10.1016/j.powtec.2010.07.025.
[57] D. Bohl, A. Mehta, N. Santitissadeekorn, E. Bollt, Characterization of Mixing in a Simple Paddle Mixer Using Experimentally Derived Velocity Fields, J. Fluids Eng. 133 (2011) 061202. doi:10.1115/1.4004086.
[58] S. Pantaleev, S. Yordanova, A. Janda, M. Marigo, J.Y. Ooi, An experimentally

validated DEM study of powder mixing in a paddle blade mixer, Powder Technol. 311 (2017) 287–302. doi:10.1016/j.powtec.2016.12.053.
[59] S.C. Thakur, J.P. Morrissey, J. Sun, J.F. Chen, J.Y. Ooi, Micromechanical analysis of cohesive granular materials using the discrete element method with an adhesive elasto-plastic contact model, Granul. Matter. 16 (2014) 383–400. doi:10.1007/s10035-014-0506-4.
[60] R. Li, X.S. Deng, J.S. Gou, Z.L. Lv, Vacuum Paddle Fast Pyrolysis Reactor Design and Internal Heat Transfer Investigation, Mater. Sci. Forum. 704–705 (2011) 468–474. doi:10.4028/www.scientific.net/MSF.704-705.468.
[61] M. Day, J.D. Cooney, Z. Shen, Pyrolysis of automobile shredder residue: An analysis of the products of a commercial screw kiln process, J. Anal. Appl. Pyrolysis. 37 (1996) 49–67. doi:10.1016/0165-2370(96)00938-2.
[62] M. Day, Z. Shen, J.D. Cooney, Pyrolysis of auto shredder residue: experiments with a laboratory screw kiln reactor, J. Anal. Appl. Pyrolysis. 51 (1999) 181–200. doi:10.1016/S0165-2370(99)00016-9.
[63] T.G. and A.M.M. E. Aylón, A. Fernández-Colino, M. V. Navarro, R. Murillo, Waste tyre pyrolysis: comparison between fixed bed reactor and moving bed reactor, Ind. Eng. Chem. Res. 47 (2008) 4029–4033.
[64] Z. Miao, T.E. Grift, A.C. Hansen, K.C. Ting, Flow performance of ground biomass in a commercial auger, Powder Technol. 267 (2014) 354–361. doi:10.1016/j.powtec.2014.07.038.
[65] J. Haydary, D. Susa, J. DudáŠ, Pyrolysis of aseptic packages (tetrapak) in a laboratory screw type reactor and secondary thermal/catalytic tar decomposition, Waste Manag. 33 (2013) 1136–1141. doi:10.1016/j.wasman.2013.01.031.
[66] E. Butler, G. Devlin, D. Meier, K. McDonnell, A review of recent laboratory research and commercial developments in fast pyrolysis and upgrading, Renew. Sustain. Energy Rev. 15 (2011) 4171–4186. doi:10.1016/j.rser.2011.07.035.
[67] Y.N. Chun, S.C. Kim, K. Yoshikawa, Pyrolysis gasification of dried sewage sludge in a combined screw and rotary kiln gasifier, Appl. Energy. 88 (2011) 1105–1112. doi:10.1016/j.apenergy.2010.10.038.
[68] M. Garcia-Perez, T.T. Adams, J.W. Goodrum, D. Geller, K.C. Das, Production and fuel properties of pine chip bio-oil/biodiesel blends, Energy and Fuels. 21 (2007) 2363–2372. doi:10.1021/ef060533e.
[69] S. Kelkar, C.M. Saffron, L. Chai, J. Bovee, T.R. Stuecken, M. Garedew, Z. Li, R.M. Kriegel, Pyrolysis of spent coffee grounds using a screw-conveyor reactor, Fuel Process. Technol. 137 (2015) 170–178. doi:10.1016/j.fuproc.2015.04.006.
[70] L. Ingram, D. Mohan, M. Bricka, P. Steele, D. Strobel, B. Mitchell, J. Mohammad, K. Cantrell, C.U.P. Jr, L. Ingram, D. Mohan, M. Bricka, P. Steele, D. Strobel, D. Crocker, B. Mitchell, J. Mohammad, K. Cantrell, C.U. Pittman, Pyrolysis of Wood and Bark in an Auger Reactor : Physical Properties and Chemical Analysis of the Produced Bio-oils Pyrolysis of Wood and Bark in an Auger Reactor : Physical Properties and Chemical Analysis of the Produced Bio-oils, Energy and Fuels. 22 (2008) 614–625. doi:10.1021/ef700335k.
[71] C.U. Pittman, D. Mohan, A. Eseyin, Q. Li, L. Ingram, E.B.M. Hassan, B. Mitchell,

H. Guo, P.H. Steele, Characterization of bio-oils produced from fast pyrolysis of corn stalks in an auger reactor, Energy and Fuels. 26 (2012) 3816–3825. doi:10.1021/ef3003922.
[72] A. Funke, D. Richter, A. Niebel, N. Dahmen, J. Sauer, Fast Pyrolysis of Biomass Residues in a Twin-screw Mixing Reactor, J. Vis. Exp. (2016) 1–8. doi:10.3791/54395.
[73] A. Funke, M. Tomasi Morgano, N. Dahmen, H. Leibold, Experimental comparison of two bench scale units for fast and intermediate pyrolysis, J. Anal. Appl. Pyrolysis. 124 (2017) 504–514. doi:10.1016/j.jaap.2016.12.033.
[74] Y. Donepudi, Impact of Pretreatment Methods on Fast Pyrolysis of Biomass, Michigan Technological University, 2017. doi:http://digitalcommons.mtu.edu/etdr/496.
[75] B.J. Klemstrud, Experimental and theoretical investigation of sustainable fast pyrolysis biofuels from woody biomass, Michigan Technological University, 2004. doi:10.3389/fmats.2017.00002.
[76] U. OSWER EPA, Advancing Sustainable Materials Management: Facts and Figures, 2016. www.epa.gov/sites/production/files/2016-11/documents/2014_smmfactsheet_508.pdf.
[77] S. Zinchik, J.L. Klinger, T.L. Westover, Y. Donepudi, S. Hernandez, J.D. Naber, E. Bar-Ziv, Evaluation of fast pyrolysis feedstock conversion with a mixing paddle reactor, Fuel Process. Technol. 171 (2018) 124–132. doi:10.1016/j.fuproc.2017.11.012.
[78] S.B. Saleh, J.P. Flensborg, T.K. Shoulaifar, Z. Sárossy, B.B. Hansen, H. Egsgaard, N. Demartini, P.A. Jensen, P. Glarborg, K. Dam-Johansen, Release of chlorine and sulfur during biomass torrefaction and pyrolysis, Energy and Fuels. 28 (2014) 3738–3746. doi:10.1021/ef4021262.
[79] S. Du, X. Wang, J. Shao, H. Yang, G. Xu, H. Chen, Releasing behavior of chlorine and fluorine during agricultural waste pyrolysis, Energy. 74 (2014) 295–300. doi:10.1016/j.energy.2014.01.012.
[80] D.S. Scott, L. Paterson, J. Piskorz, D. Radlein, Pretreatment of poplar wood for fast pyrolysis: Rate of cation removal, J. Anal. Appl. Pyrolysis. 57 (2001) 169–176. doi:10.1016/S0165-2370(00)00108-X.
[81] M.J. Antal, Effects of Reactor Severity on the Gas-Phase Pyrolysis of Celulose- and Kraft Lignin-Derived Volatile Matter, Ind. Eng. Chem. Prod. Res. Dev. 22 (1983) 366–375. doi:10.1021/i300010a039.
[82] M.M. Wright, D.E. Daugaard, J.A. Satrio, R.C. Brown, Techno-economic analysis of biomass fast pyrolysis to transportation fuels, Fuel. 89 (2010) S2–S10. doi:10.1016/j.fuel.2010.07.029.
[83] D. Carpenter, T.L. Westover, S. Czernik, W. Jablonski, Biomass feedstocks for renewable fuel production: A review of the impacts of feedstock and pretreatment on the yield and product distribution of fast pyrolysis bio-oils and vapors, Green Chem. 16 (2014) 384–406. doi:10.1039/c3gc41631c.
[84] P. Thy, C. Yu, B.M. Jenkins, C.E. Lesher, Inorganic composition and environmental impact of biomass feedstock, Energy and Fuels. 27 (2013) 3969–3987.

doi:10.1021/ef400660u.
[85] I. Obernberger, F. Biedermann, Fractionated heavy metal seperation in biomass combustion plants as a primary measure for sustainable ash utilization, in: A. V. Bridgwater (Ed.), Dev. Thermochem. Biomass Convers., Springer Science+Business Media Dordrecht, Netherlands, 1997: pp. 1368–1369.
[86] Z. Dobó, A. Fry, Investigation of co-milling Utah bituminous coal with prepared woody biomass materials in a Raymond Bowl Mill, Fuel. 222 (2018) 343–349. doi:10.1016/j.fuel.2018.02.181.
[87] J.A. Luppens, A critical review of published coal quality data from the southwestern part of the Powder River Basin, Wyoming, USGS. (2011) 23.
[88] S. Guo, L. Zhang, X. Niu, L. Gao, Y. Cao, X.X. Wei, X. Li, Mercury release characteristics during pyrolysis of eight bituminous coals, Fuel. 222 (2018) 250–257. doi:10.1016/j.fuel.2018.02.134.
[89] F.P. Incropera, D.P. DeWitt, Fundamentals of heat and mass transfer, J Wiley, New York, 2002.
[90] P.E. Mason, L.I. Darvell, J.M. Jones, A. Williams, Comparative Study of the Thermal Conductivity of Solid Biomass Fuels, Energy and Fuels. 30 (2016) 2158–2163. doi:10.1021/acs.energyfuels.5b02261.
[91] B. Insider, Density of selected plastic materials that float or sink in relation to seawater density, Stat. - Stat. Portal. (n.d.). https://www.statista.com/statistics/595434/pl (accessed October 7, 2018).
[92] A. Ullal, Heat transfer analysis in a paddle reactor for biomass fast pyrolysis, Michigan Technological University, 2017. doi:http://digitalcommons.mtu.edu/etdr/313.
[93] Z. Xu, S. Zinchik, S.S. Kolapkar, E. Bar-Ziv, T. Hansen, D. Conn, A.G. McDonald, Properties of Torrefied U.S. Waste Blends, Front. Energy Res. 6 (2018) 1–13. doi:10.3389/fenrg.2018.00065.
[94] F.A. Miller, Spectra of carbonyl compounds of all kinds (factors affecting carbonyl group frequencies), John Willey and Sons, Inc, 2003. doi:https://doi.org/10.1002/0471690082.ch1.
[95] F. Stankovikj, A.G. McDonald, G.L. Helms, M. Garcia-Perez, Quantification of Bio-Oil Functional Groups and Evidences of the Presence of Pyrolytic Humins, Energy and Fuels. 30 (2016) 6505–6524. doi:10.1021/acs.energyfuels.6b01242.
[96] S. Liang, Y. Han, L. Wei, A.G. McDonald, Production and characterization of bio-oil and bio-char from pyrolysis of potato peel wastes, Biomass Convers. Biorefinery. 5 (2015) 237–246. doi:10.1007/s13399-014-0130-x.
[97] L. Wei, S. Liang, N.M. Guho, A.J. Hanson, M.W. Smith, M. Garcia-Perez, A.G. McDonald, Production and characterization of bio-oil and biochar from the pyrolysis of residual bacterial biomass from a polyhydroxyalkanoate production process, J. Anal. Appl. Pyrolysis. 115 (2015) 268–278. doi:10.1016/j.jaap.2015.08.005.
[98] Y. Han, D.N. McIlroy, A.G. McDonald, Hydrodeoxygenation of pyrolysis oil for hydrocarbon production using nanospring based catalysts, J. Anal. Appl. Pyrolysis. 117 (2016) 94–105. doi:10.1016/j.jaap.2015.12.011.

Appendix

The publication in *Frontiers in Energy Research* journal by author is attached below. It is cited as:

Z. Xu, S. Zinchik, S.S. Kolapkar, E. Bar-Ziv, T. Hansen, D. Conn, A.G. McDonald, Properties of Torrefied U.S. Waste Blends, Front. Energy Res. 6 (2018) 1–13. doi:10.3389/fenrg.2018.00065.

frontiers in Energy Research

ORIGINAL RESEARCH
published: 13 July 2018
doi: 10.3389/fenrg.2018.00065

Properties of Torrefied U.S. Waste Blends

Zhuo Xu[1], Stas Zinchik[1], Shreyas S. Kolapkar[1], Ezra Bar-Ziv[1], Ted Hansen[2], Dennis Conn[2] and Armando G. McDonald[3]*

[1] Department of Mechanical Engineering, Michigan Technological University, Houghton, MI, United States, [2] Convergen Energy LLC, Green Bay, WI, United States, [3] Department of Forest, Rangeland and Fire Sciences, University of Idaho, Moscow, ID, United States

Power generation facilities in the U.S. are looking for a potential renewable fuel that is sustainable, low-cost, complies with environmental regulation standards and is a drop-in fuel in the existing infrastructure. Although torrefied woody biomass, meets most of these requirements, its high cost, due to the use of woody biomass, prevented its commercialization. Industrial waste blends, which are also mostly renewable, are suitable feedstock for torrefaction, and can be an economically viable solution, thus may prolong the life of some of the existing coal power plants in the U.S. This paper focuses on the torrefaction dynamics of paper fiber-plastic waste blend of 60% fiber and 40% plastic and the characterization of its torrefied product as a function of extent of reaction (denoted by mass loss). Two forms of the blend are used, one is un-densified and the other is in the form of pellets with three times the density of the un-densified material. Torrefaction of these blends was conducted at 300°C in the mass loss range of 0-51%. The torrefied product was characterized by moisture content, grindability, particle size distribution, energy content, molecular functional structure, and chlorine content. It was shown that although torrefaction dynamics is of the two forms differs significantly from each other, their properties and composition depend on the mass loss. Fiber content was shown to decrease relative to plastic upon the extent of torrefaction. Further, the torrefied product demonstrates a similar grinding behavior to Powder River Basin (PRB) coal. Upon grinding the fiber was concentrated in the smaller size fractions, while the plastic was concentrated in the larger size fractions.

Keywords: waste, fiber, plastic, torrefaction, grindability, energy content, chlorine content, FTIR spectroscopy

OPEN ACCESS

Edited by:
Allison E. Ray,
Idaho National Laboratory (DOE), United States

Reviewed by:
Muhammad Aziz,
Tokyo Institute of Technology, Japan
Maria Puig-Arnavat,
Technical University of Denmark, Denmark

***Correspondence:**
Ezra Bar-Ziv
ebarziv@mtu.edu

Specialty section:
This article was submitted to Bioenergy and Biofuels, a section of the journal Frontiers in Energy Research

Received: *12 April 2018*
Accepted: *19 June 2018*
Published: *13 July 2018*

Citation:
Xu Z, Zinchik S, Kolapkar SS, Bar-Ziv E, Hansen T, Conn D and McDonald AG (2018) Properties of Torrefied U.S. Waste Blends. Front. Energy Res. 6:65. doi: 10.3389/fenrg.2018.00065

INTRODUCTION

The U.S. Environmental Protection Agency (EPA) has accelerated regulatory pressure on utilities burning pulverized coal by issuing carbon emission guidelines on June 18, 2014 (EPA, 2014). The EPA has proposed state by state goals to achieve CO_2 emission reductions; 30% from the power sector as compared to CO_2 emission levels in 2005 (EPA, 2015). The ultimate fate and form of the EPA proposed rule may not be known for some time until the rule-making process is complete but the past history of utility emissions regulation and Supreme Court decisions on EPA rule-making authority indicate a high probability that some form of CO_2 regulation will be implemented (White, 2014). Internationally, the U.S. has announced the reduction of greenhouse gas emissions by 26–28% below 2005 levels by 2025 (Nakamura and Mufson, 2014).

Torrefied-biomass is a high-energy fuel that can be used in combustion, gasification, and pyrolysis, and is considered either fully or partially renewable and complies with the above EPA regulations (EPA, 2015). Kiel (Kiel, 2011) suggested the use of biomass for coal power plants. Potential users of torrefied biomass are suggested for refineries to produce bio-oil (Wang et al., 2016; De Rezende Pinho et al., 2017) and syngas producers (TRI, 2018). A considerable amount of studies, pilot-scale plants, patents and commercial efforts have been devoted to torrefaction and torrefied materials. The entries "torrefaction" and "torrefied" in the title, shows 790 papers, 19 reviews, and 50 patents, between 1990 and 2017. The 50 patents comprise many technologies for torrefaction, most of which are based on mechanical mixing. Although torrefaction technology is well developed, it has not yet moved to the commercial market. The consensus is that the main hindrance to the commercialization of this technology is the use of high-cost woody biomass as a feedstock (Kumar et al., 2017; Radics et al., 2017).

The use of wastes (for example, municipal solid wastes—MSW—or industrial manufacturing residuals—fiber and plastic blends) can be the answer to the deployment of this technology as tipping fees are paid for the waste destined for landfill. U.S. wastes possess substantial energy content that can be utilized for energy and power (US-EIA, 2010). Wastes, as a feedstock in torrefaction, has been suggested by Bar-Ziv and Saveliev (2013) and Bar-Ziv et al. (2016) and others, using regular torrefaction (Yuan et al., 2015), wet torrefaction (Mumin et al., 2017), and microwave torrefaction (Iroba et al., 2017a,b). Some difficulties have been recognized while using waste for torrefaction because of difficulties in conveying, pretreatment and potential emissions. Other hurdles were also identified while using waste feedstocks in torrefaction: (i) inconsistency in feedstock, (ii) possibility of high Cl, S, and N content, (iii) binders required for compaction of torrefied biomass (Bar-Ziv and Saveliev, 2013; Bar-Ziv et al., 2016), (iv) high moisture content in MSW and the like, and (v) high contaminant content that leads to emissions issues.

The EPA regulatory actions (EPA, 2014, 2015) regarding the use of alternative fuels raise the likelihood that torrefied waste will find a market to replace pulverized coal in energy production. One other recent development affecting the market for torrefied biomass from MSW was a memorandum from the EPA's Office of Air and Radiation addressing the framework for determining the carbon neutrality of biomass (McCabe, 2014).

There is a significant amount of waste in the U.S., which is being disposed of in landfills, that can be used as an energy source. **Table 1** summarizes the various wastes, totaling ~110,000 ton per year, as well as their calorific values. This significant amount, if torrefied, can replace coal and be considered renewable and clean fuel. From an energy perspective, except plastic wastes with very high heat content ~ 36 MJ/kg, the rest have heat values in the range 15–17 MJ/kg. The weighted average heat content in U.S. waste is ~21 MJ/kg, which is comparable to that of Powder River Basin (PRB) coal that has a heat content of ~17–19 MJ/kg (Luppens, 2011). This indicates that 1 dry ton of U.S. waste can replace 1 ton of PRB coal. With current coal consumption of ~650,000 tons/d of coal in the US (with over 50% PRB coal) (US-EIA, 2018), U.S. waste could replace well over 15% of the U.S. coal.

TABLE 1 | U.S. wastes, quantities, and heat content.

Waste type	Quantity, in 1000 ton (EPA, 2016)	%	Heat content (db), MJ/kg	Source
Paper	19,470	18	14.7	Demirbas, 1999
Plastic	25,100	23	35.7	Themelis and Mussche, 2014
Rubber and leather	4,150	4	36.5	Unapumnuk et al., 2006
Textile	10,000	9	17	Miranda et al., 2007
Wood	11,010	10	15-16	McKendry, 2002
Food	29,319	27	15–16	US-EIA, 2010
Yard trimmings	10,790	10	15–16	McKendry, 2002
Total	109,839	100		

The present paper deals with torrefaction of certain U.S. wastes, including plastics, which can be converted into drop-in fuels as a replacement of coal in coal power plants. Specifically, the paper deals with wastes blends from paper/carton (wood fibers) and plastics. As such, the torrefied fuel should be shown to match the characteristics and properties of coals.

MATERIALS AND METHODS

Materials

Convergen Energy (CE) developed a fuel engineering process: sorting and blending feedstocks of fiber and plastic, removing metal and shredding down to 25 mm by 1 mm flakes by which waste blends of fibers (from paper, label matrix residuals, and laminated non-recyclable papers/plastics and the like) and plastics, become uniform, flowable and consistent, with a bulk density in the range 200–300 kg/m^3. CE also developed a pelletization process that produces pellets (12 mm OD and 50 mm long) that are rather uniform with a density of 750–800 kg/m^3 and bulk density of 400–450 kg/m^3. The binder for the CE palletization process was the plastic component in the blend. CE characterized their product for over 7 years with properties that showed rather consistent products. **Table 2** shows average properties of waste blends of 60% fiber with 40% plastics, with standard deviations of its product over a 7-year period. As seen, the properties in **Table 2** are indicative of reproducible and consistent material. This material was the feedstock in the torrefaction process, both in un-densified and densified forms.

In this study, both the un-densified as well as the densified material (pellets indicated above) were used. **Figure 1** shows both forms before torrefaction, used in this study: (a) un-densified CE material; and (b) CE pellets.

Waste and Product Characterization

The properties depicted in **Table 2** are part of the routine characterization of CE products, both before and after

TABLE 2 | Properties of CE material averaged over a 7-year period.

Proximate	Values	Ash	Values, %	Others	Values, ppm	Fusion temp	Value °C
Moisture, %	3.3 ± 0.5	SiO_2	33 ± 18	Cl	1162 ± 487	**Reducing**	
Ash, %	6.0 ± 0.6	A_2O_3	27 ± 11	F	75 ± 75	Deformation	1,319
Volatiles, %	83.5 ± 2.6	TiO_2	7.2 ± 3.4	Hg	0.01 ± 0.01	Softening	1,359
Fixed Carbon, %	7.2 ± 2.0	Fe_2O_3	0.9 ± 0.9	Sn	2.9 ± 0.9	Hemispherical	1,374
Sulfur, %	0.2 ± 0.1	CaO	21 ± 12	As	1.1 ± 0.9	Fluid	1,396
HHV, MJ/kg	26.10 ± 1.05	MgO	3.0 ± 3.0	Be	0.3 ± 0.8	**Oxidizing**	
Ultimate	**Values, %**	K_2O	0.6 ± 0.4	Cr	2.2 ± 1.2	Deformation	1,327
Carbon	55.4 ± 1.8	Na_2O	1.6 ± 0.7	Co	0.21 ± 0.16	Softening	1,369
Hydrogen	7.9 ± 0.3	MnO_2	0.02 ± 0.01	Pb	1.1 ± 1.4	Hemispherical	1,384
Nitrogen	0.3 ± 0.1	BaO	0.2 ± 0.2	Ni	0.81 ± 0.57	Fluid	1,406
Oxygen	27.1 ± 1.6	Others	2.8 ± 1.4	Se	1.5 ± 1.8		

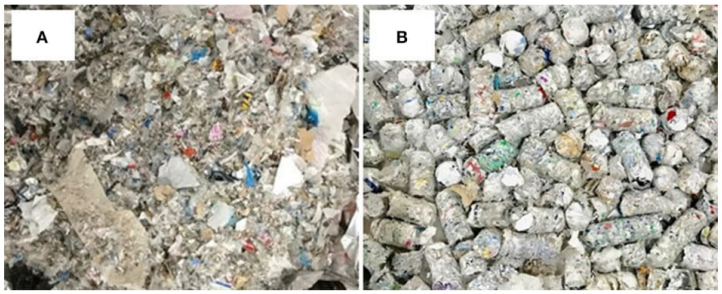

FIGURE 1 | (A) Un-densified CE material. **(B)** Densified (pellets) CE material.

pelletization. Other characterization methods are as follows. All data presented in this paper were averaged over 3–5 data points.

Grinding

Grindability is an important characteristic that has an essential impact on the applicability of torrefied material as a drop-in fuel in coal power plants. Typically, coal power plant use pulverizers of type MPS 89 (Storm, 2009), however, for the grinding tests, blade grinders (that operate at 24,000 rpm) were used. The grinding results presented in this paper are for comparison purposes. Two blade grinders were used in this study: Model CIT-FW-800 and Model CIT-FW-200. An on-line power meter—Wattsup pro was used for power vs. time measurements. Also, note that CE material was torrefied in both non-densified and densified (pellets) forms and grinding tests were carried out for both materials. Two types of grinding tests were performed as follows:

(1) A 100–200 g torrefied sample (either un-densified or pellet form) was placed in the grinder, which was continuously operated for up to 120 s time interval (to avoid damage to the motor); the power was measured continuously during the experiment. If necessary, grinding was repeated in a similar manner for a total of 1,800 s.

(2) A 100–200 g torrefied sample was placed in the grinder and operated for short time intervals – 15–30 s. After each grinding run (time interval) the pulverized material was sifted to seven sizes, in the range of 150–2,000 μm, after which all size fractions were mixed and were further pulverized for another time interval. This process was repeated until the size fractions reached asymptotic values.

In both methods, the power was measured with and without the sample in the grinder. The power without the sample was subtracted from that with the sample, which provided the net power required to grind the sample. **Figure 2** shows a typical plot of power vs. time with and without a sample (in this case, 200 g of a torrefied non-densified material at 21.4% mass loss during torrefaction). Note that the startup is accompanied by an overshoot, in both cases.

Sifting

Sifting of the pulverized material was carried out in a W.S Tyler, RX-86 model sieve shaker. Seven size fractions were obtained with screen sizes of 75, 150, 180, 250, 425, and 850 μm. At each time interval after grinding, all the material inside the grinder was taken out and put into the shaker to sift for an hour. The weights of all the screens before and after the sifting were measured. The

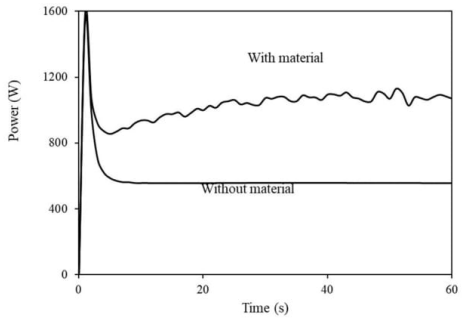

FIGURE 2 | Examples of power vs. time traces of the grinder without material and with 200 g torrefied un-densified material.

difference in these weights provided the sample weight of each size fractions.

Chloride and Chlorine

The chloride dissolved liquid samples from high shear mixing (described below) were diluted by a factor of hundred. Chloride was measured in this aqueous solution using Milwaukee Instruments, MI414 model Chloride Professional Photometer. Two cuvettes were used for the experiments. One is the blank sample filled with 10 ml of distilled water and another cuvette filled with 10 ml of diluted liquid sample. Then 0.5 ml of reagent-1 (Thiocyanate and Mercury) was added to both cuvettes, and after 30 s of swirling, 0.5 ml of reagent-2 (Nitric Acid) was added to both cuvettes. After another 30 s of swirling, the blank sample was first measured and zeroed, then the liquid sample was inserted in Chloride photometer which directly showed the chloride content of the liquid sample.

Total Chlorine in the solid phase was measured using the ASTM D4208-1 standard. The testing process included following key steps: The weighed solid sample was burned in a bomb filled with 2–3 MPa oxygen. After the combustion, a diluted base solution (2% Na_2CO_3 solution) was added to the bomb to react with the chloride product. Water was then used to wash the inside cylinder wall of the bomb. All the washings were collected in a beaker and the ionic strength was adjusted using ($NaNO_3$ solution) (Zhu, 2014). The total chloride content of the solid material is determined by measuring the potential of the solution with a chlorine ion-selective electrode using a potentiometric titration (916 Ti-Touch) with silver nitrate solution.

Heat Content

Heat content was measured by Parr 6100 Compensated Jacket Calorimeter, where 1 g samples was placed inside sampling bowl/tray, and the sample was connected to the electric circuit using fuse string. This setup was put into a bomb and then filled with oxygen. The bomb was then put into a bucket with 2,000 ±0.5 g of distilled water. The process involved ignition of sample using an ignition circuit and subsequent measurement of temperature difference after the burning of the measured sample. The heating value was displayed by the calorimeter based on the calibration and temperature difference.

Moisture Content

Moisture content was measured using HFT-1000 moisture analyser. Around 1 g of sample was put into the analyser. After starting the analysis, the heating coil would heat up and the moisture inside the material would volatilize. The analyser would show the moisture content by measuring the difference of the weight before and after the experiment. Moisture content was measured before and after torrefaction. The values were rather consistent, before torrefaction moisture was in range 2–3% and after torrefaction, 0%.

Density Measurements

Density measurement of pellets was done using a scale (model A&D HR-60) with readability of 0.0001 g. The Archimedes' principle/buoyancy method was used for density measurement. A simple stand with suspended metal wire setup was used to dip the pellet in water. The procedure followed was as below:

1. The pellet was placed on scale and dry weight, w, was noted.
2. A beaker filled with set level of distilled water was placed on the scale and tared zero.
3. The stand and wire setup were placed next to scale such that some part of wire dipped in the water. The scaled was tared zeroed again.
4. The sample was attached to wire and the sample was dipped in water. Care was take that entire sample dipped in well and did not touch bottom of the beaker. The reading with suspended sample, w_s, was noted.
5. The density was obtained by taking the ratio of suspended sample weight, w_s and dry weight w.

FTIR

FTIR spectra were obtained on (i) 20 randomly selected pieces of mixed waste and (ii) screened fractions of the torrefied material (in triplicate) using a Nicolet-iS5 FTIR spectrometer, 64 scans, with an attenuated total reflectance accessory (ZnSe crystal, iD5) and data analyzed and averaged with the OMNIC v9.8 software and Aldrich, Hummel, and Nicolet spectral libraries. Carbonyl index (CI), cellulose index (CeI), and hydroxyl index (HI) were calculated as the ratio of the band intensity (absorbance) at 1,720, 1,024, and 3,342 cm^{-1}, respectively, to the band 2,916 cm^{-1} for the -CH2- groups (Wei et al., 2013).

Experiments

Torrefaction

Torrefaction experiments were carried out by placing a sample, motionless, at the center of a convection furnace, Lindenberg/Blue type BF51828C-1, with flow of inert gas, either N_2 or CO_2 to avoid oxidation of the material. For un-densified CE material, typically samples of 150 g were placed in a thin aluminum foil at the furnace center, with residence time in the range 1–40 min. For CE pellets, sample size was ~300 g and torrefaction residence time was between 3 and 120 min.

Removal of Soluble Minerals

Soluble minerals in the torrefied material were removed by a method developed by Donepudi (Donepudi, 2017). In the present study, a 7.5 g torrefied sample was placed in a high shear mixer of Charles Ross & Son Company (Model HSM-100LSK-1) where water was added to the sample in 20:1 ratio by weight and the mixer was rotated at ∼7,000 rpm for 5 min. A suspension generated was filtered by 11 μm porosity paper filter (Whatman 1001-0155 quantitative filter paper circles), followed by another filtration by 1.6 μm porosity paper filter (Whatman 1820-047 glass microfiber binder free filter). The two filtration processes produced a transparent solution with no apparent suspend particles or colloids. The aqueous solution was measured for chloride as described above.

RESULTS

Torrefaction

As mentioned, all current torrefaction experiments were carried out by introducing un-densified material and pellets in a convective furnace at 300°C, with the initial temperature of the particle, T_o, at ambient temperature. The material was placed in the furnace center and was kept stationary. In this case, the particle was heated by heat transported from the hot walls at temperature (T_w) to the particle surface by convection; the heat was then transported into the particle by conduction. Numerous torrefaction experiments were carried out for pellets as well un-densified material. In both cases, the results show clear trends, with a delay in the onset of mass loss followed by an increase in the mass loss with time. The dynamic behavior in the two cases differed significantly from each other; for the un-densified material, the mass loss starts at around 3 min, whereas for the pellets, it starts at around 9 min. Further, for the un-densified material, mass loss increase with time was faster compared to pellets. This behavior was indicative to the heat-transfer-chemical-reaction system. To determine the regime that best fits the description of the system behavior, one should start with the analysis with Biot number (*Bi*) and thermal Thiele modulus (*M*); the former is related to the heating regime of the particle, and the latter relates to the propagation of the torrefaction reaction within the particle. The *Bi* and *M*, which are defined as:

$$Bi = \frac{h}{\lambda / L_c} \tag{1}$$

$$M = \frac{R^{\dagger}}{\lambda / (c_p L_c^2)} \tag{2}$$

where h is the convective heat transfer coefficient, λ is the particle thermal conductivity, L_c is the particle characteristic length, $R^{\dagger}$ is the torrefaction reaction rate within the particle, c_p is the particle heat capacity, and ρ is particle density. The parameters required to determine *Bi* and *M* from Equations (1) and (2) are not easy to determine as the material is not well defined and therefore, can only provide an estimate. The value of heat transfer coefficient, h, was selected to be 10 (W/m^2-K) and was the closest to the flow conditions prevailing in the furnace (Incropera and DeWitt, 2002). The value for thermal conductivity, λ, varies between 0.15 (W/m-K) for PVC, and 0.38 (W/m-K) for polyethylene (Incropera and DeWitt, 2002; Patterson and Miers, 2010); for biomass and fibers the values range in 0.03–0.29 (W/m-K) (Mason et al., 2016). A value of 0.2 (W/m-K) was selected which was an average of the above. Literature data on reaction rates of the material used were even more scattered than thermal conductivity, therefore they were measured by thermogravimetry in the furnace. The rate of mass loss of the CE material from both measurements at 300°C was about 0.03%/s, where the material temperature has been equal to the wall temperature (T_w); using the density of each form to obtain a value of 0.2–0.3 (kg/m^3-s) for the un-densified material and 0.1–0.2 (kg/m^3-s) for the pellets. In this study, the density was 1,150 (kg/m^3) for the un-densified material and 850 (kg/m^3) for the pellets. Heat capacity was both taken from the literature (Incropera and DeWitt, 2002) and measured to yield an acceptable value of 1,600 (J/kg-K) (Donepudi, 2017). The characteristic lengths of the two forms were measured (very accurately for the pellets and rather scattered for the un-densified material). **Table 3** summarizes all properties required for the determination of *Bi* and *M*, yielding values for (i) *Bi* of ∼0.1 for the un-densified material and ∼0.35 for the pellets and (ii) *M* of ∼0.01 for the un-densified material and ∼0.08 for the pellets. The values for *Bi* in the range 0.1–0.35 indicate that the rate of heat transfer by convection from the furnace walls to the particle was lower than the rate of heat transfer into the particle. The values of *M* are in the range 0.01–0.08 which indicate that the reaction rate was significantly slower than the heat transfer into the particle, and the particles equilibrate its temperature faster than the reaction rate. This analysis indicates that the reaction propagation was controlled by the rate of heat transfer from the furnace walls to the particle surface, after which the particle temperature equilibrates instantly.

Establishing that the torrefaction reaction rate was controlled by the heat transfer from the walls to the particle surface and that the particle temperature was uniform at all times, means that the reaction propagates with the rate of ramp-up of the particle temperature. To calculate the particle temperature, the equation of the heat rate, *dQ(t)/dt*, from the walls to the particle surface was needed to be solved, which was equal to

$$\frac{dQ(t)}{dt} = hA\left[T_w - T_s(t)\right] \tag{3}$$

where T_w and $T_s(t)$=$T(t)$ are wall and particle surface (or particle) temperatures, respectively. $Q(t)$ is the heat required to increase the particle temperature, or

$$Q(t) = mc_p\left[T(t) - T_o\right] + mh_r \tag{4}$$

where m and c_p are particle mass and specific heat capacity, respectively, T_o is the particle core temperature, which is also equal to the initial temperature of the particle, and h_r is enthalpy of reaction. It was a challenge to find values for h_r as the torrefied material was not well defined, it comprises

TABLE 3 | Estimated values for the parameters to determine the Bi and M.

Parameter	Value	Source
h, W/m^2-K	10	Incropera and DeWitt, 2002
λ for CE material, W/m-K	0.2	Incropera and DeWitt, 2002
$R^{\dagger}$ for un-densified material, kg/m^3-s	0.3	Measured in current study
$R^{\dagger}$ for pellets, kg/m^3-s	0.2	Measured in current study
ρ for un-densified material, kg/m^3	1,150	Measured in current study
ρ for pellets, kg/m^3	850	Measured in current study
c_p, J/kg-K	1,600	Incropera and DeWitt, 2002; Donepudi, 2017
L_c thickness for un-densified material, m	0.002	Measured in current study
L_c diameter for pellets, m	0.007	Measured in current study
Bi for un-densified material	0.1	Current result
Bi for pellets	0.35	Current result
M for un-densified material	0.01	Current result
M for pellets	0.08	Current result

fibers (mostly cellulose) and a large variety of plastic materials. Cellulose torrefaction in the 25–300°C temperature range starts as an endothermic reaction and continues as an exothermic reaction (Bates and Ghoniem, 2013). Enthalpies of reaction for plastic in the same temperature range were always positive and vary in the range (12.55–147.86 J/kg) (Zhao et al., 2017), which is smaller than the value of $c_p(T\text{-}T_o)$ (~400 kJ/kg) in Equation (4). Thus, for simplification, this term was ignored. Introducing Equation (4), without h_r, into Equation (3) and integration from T_w to $T(t)$ yields

$$\frac{T_w - T(t)}{T_w - T_o} = e^{-t/\tau} \tag{5}$$

where τ is a characteristic time, defined as

$$\tau = \frac{mc_p}{hA} \tag{6}$$

For the pellets (cylinders), $\tau_{cyl} = d\rho c_p/4h$ (d is cylinder diameter, ρ is particle density) and for the un-densified material (slab) it is $\tau_{slab} = d\rho c_p/2h$ (d is slab thickness). Rearrangement of Equation (5) yields

$$T^*(t) = 1 - (1 - \frac{T_o}{T_w})e^{-t/\tau} \tag{7}$$

T^* is defined as

$$T^*(t) = \frac{T(t)}{T_w} \tag{8}$$

To model the mass loss, the torrefaction reaction rate was assumed to be represented by a first order rate, which a rather common assumption in many torrefaction studies (Lédé, 2010; Funke et al., 2017), or

$$R^{\dagger} = \rho\frac{d\alpha(t)}{dt} = -\rho k\alpha(t) \tag{9}$$

where $a{=}m/m_o$ is ratio of mass-to-initial-mass, k is rate coefficient assumed to follow an Arrhenius behavior,

$$\rho k(T) = A^{\dagger}e^{-T_a/T(t)} \tag{10}$$

where $A^{\dagger}$ is a pre-exponential factor and T_a is a characteristic temperature equals $T_a = E_a/R$, E_a is activation energy and R is gas constant. Introducing Equation (10) into Equation (9) and integrating yields an expression for the mass loss, $1\text{-}\alpha$, equals

$$1 - \alpha = 1 - (A^{\dagger}/\rho)e^{-T_a/T(t)} \tag{11}$$

The required values for determining τ, Equation (6), for each case are given in **Table 3**. Introducing these values in Equation (6) yields $\tau_{slab} = 184$ (s) and $\tau_{cyl} = 475$ (s), the subscript *slab* is for the un-densified material and *cyl* is for the pellets. Using these values, the particle temperatures were calculated and presented in **Figure 3**. As noted, the particle temperature in the un-densified case increases much faster than that of the pellets. Note from **Figure 3** the temperature of the un-densified material reaches the wall temperature after 10 min, whereas for the pellets, it reaches the wall temperature after 30 min.

The values for $(A^{\dagger}/\rho)$ and T_a were determined by fitting the model results for mass loss of Equation (11), using the temperature transients of Equation (7) (**Figure 3**), to the experimental results. **Figure 4** shows the measured mass loss vs. time data (scattered results) and the model results using Equation (11). Clearly, the model results yielded an excellent fit to the experimental data. The fitting process yielded for the un-densified material (slab) values of $(A^{\dagger}/\rho)_{slab} = 1.23x10^8$ and $(T_a)_{slab} = 15{,}200$ (K), and for the pellets (slab) values of $(A^{\dagger}/\rho)_{slab} = 1.08x10^8$ and $(T_a)_{cyl} = 15{,}800$ (K). The values of $A^{\dagger}/\rho$ and T_a for both forms of materials are very close to each other which is a strong indication that the model proposed here is representing the actual system behavior rather well.

Grinding Energy

The method of determining the grinding behavior has been explained above, with power that was continuously measured as a function of time during grinding for a given sample weight. Numerous grinding tests were conducted, in the mass loss range 10–51%, for the two forms of torrefied materials: un-densified and pellets. All net power transient results portrayed distinct behavior that showed two characteristic time: short and much longer. Further, the net grinding power transients for all samples fitted a double exponential rise of the form:

$$P(t) = a_1(1 - e^{-t/\tau_1}) + a_2(1 - e^{-t/\tau_2}), \tag{12}$$

where τ_1 and τ_2 are the short (1) and long (2) characteristic times, respectively, and a_1 and a_2 are the asymptotic values of the power for the short and long characteristic times, respectively.

Figure 5 shows typical examples of the measured (symbols) net power vs. time of two 200 g samples during grinding of torrefied CE, un-densified material and pellets and fits (dashed lines) of the net power to Equation (12). In both cases, the short characteristic time was found $\tau 1 = 9.2$ s and characteristic time $\tau 2 = 203$ s.

All results for the torrefied samples and pellets in the range 10–51% mass loss were fitted to Equation (12) to yield: for the short characteristic time of $\tau 1 = 9.1 \pm 0.5$ s, and for the long time it was $\tau 2 = 203 \pm 10$ s with the respective asymptotic values of a1 = 378.1 W and a2 = 73.0 W that varied within ±5%. To demonstrate the general behavior of torrefied samples, **Figure 6** shows normalized net grinding power (by the asymptotic values) vs. time for the short time range, showing clearly identical behavior for all samples tested. The dashed line in the figure is a unity line that shows the normalized asymptotic value. The fact that the grinding dynamics is characterized by two characteristic times, that significantly differ from each other, indicates clearly that there are two materials. A detailed discussion of these two materials is given in the energy content section below.

As will be shown below, most of the material was ground in the short time range, thus a characteristic grinding energy can be determined by integrating the power over a certain time, which we selected as 1 τg, 2 τg, and 3 τg (or, 8.1 s, 16.2 s, 24.3 s). **Table 4** shows the values of the specific grinding energy for three characteristic grinding time, 1 τg, 2 τg, 3 τg, where

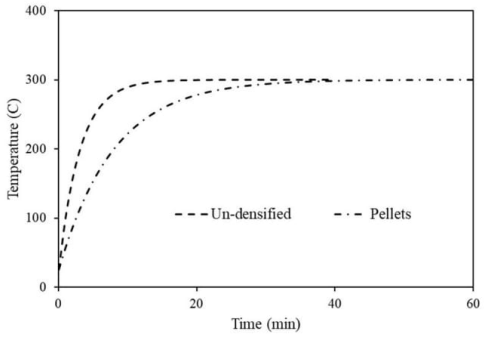

FIGURE 3 | Temperature transient for the un-densified material and the pellets, using Equation (7) and characteristic times of 160 (s) for the former and 475 (s) for the later.

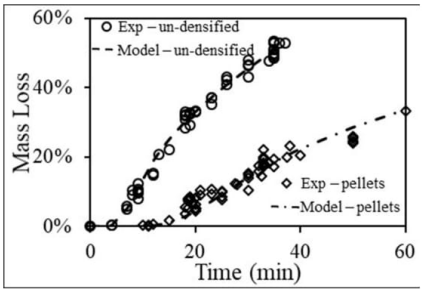

FIGURE 4 | Experimental and modeled mass loss transients for the un-densified material and the pellets, using Equation (11), the temperature transients of **Figure 3** and fitting for T_a and $A^{\dagger}$.

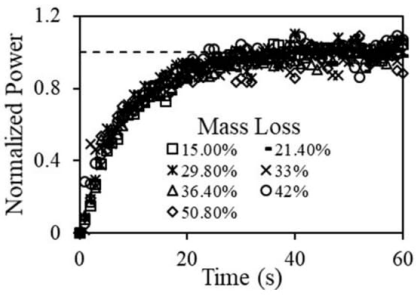

FIGURE 6 | Normalized net grinding power vs time for torrefied material at various mass losses; with τg = 9.1 (s).

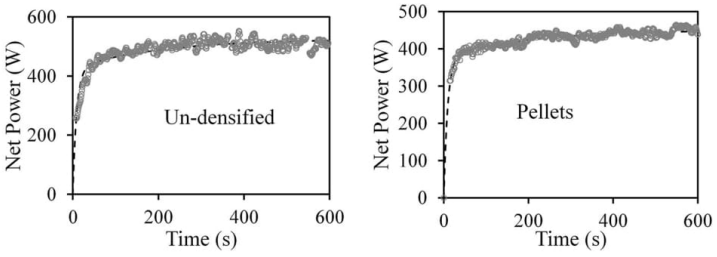

FIGURE 5 | Symbols—measured net power vs. time of 200 g samples during grinding of torrefied CE, un-densified material and pellets. Dashed lines, fits of net power to Equation (12) for the short characteristic time, $\tau_1 = 9.2$ s; and characteristic time $\tau_2 = 203.0$ s.

τg =8.1 (s) in kJ/kg and in commonly used kWh/ton units. As expected, the specific grinding energies increases strongly with the integration time. The values determined here are similar to values obtained in other studies at 8.23 kWh/ton (Khalsa et al., 2016). For comparison, grinding characteristics of PRB were also studied with power vs. time results for a 200 g PRB coal sample shown in **Figure 7**. A fit of these results with a characteristic grinding time, τg, of 8.1 was done and specific grinding energies were calculated as shown in **Table 4**. The values for the specific grinding energies for the torrefied (un-densified) material are within the experimental uncertainty to those of the PRB coal and smaller than the energy required to grind the torrefied biomass (Wang et al., 2017).

Sizing Distribution

Many sifting experiments were done as a function of grinding time (or grinding energy), where the samples were sifted in size range 150 μm−3 mm in 5 size fractions: x<150 μm, 150<x<250 μm, 250<x<425 μm, 425<x<850 μm, x>850 μm (x denote size). It was observed that after reaching steady state (i.e., the net grinding power reached an asymptotic value), the size distribution did not change anymore. Therefore, most of the sifting experiments were done after reaching grinding steady state. The initial sample was around 100 grams, and after grinding and sifting, there was ∼1 g of sample loss during the transferring procedure, which occurred only once during the process. Therefore, loss was not more than 1%. Although there is scatter in the results, there are clear trends: the size fraction >850 μm decreased with mass loss and the size fraction <150 μm increased with mass loss and the size fractions in between did not change much with mass loss. Therefore, the behavior in two size fractions: under and above 850 μm was further investigated. **Figure 8** shows size fraction as a function of mass loss for the torrefied un-densified material and pellets for these two size fractions. It is interesting to note that for each size fraction, the dependence on mass loss is rather similar (the line is a fit to a straight line). For the size under 850 μm, its fraction starts at 82% for 4.5% mass loss and reaches almost 100% at 51% mass loss, the size fraction above 850 μm balances the smaller size fraction. **Table 5** shows fraction >200 mesh of pulverized torrefied material at various mass losses. The table indicates that above 8.4% mass loss, after grinding the fraction of <200 mesh is >70%, which is consistent with of the typical coal power plant requirements (Helble et al., 1990).

FTIR Spectroscopic Characterization

The CE waste mix plus fiber (20 random pieces selected) was analyzed by FTIR spectroscopy to determine their chemical identity with spectra library matching. The mix was shown to be comprised of three cellulose/paper, three polypropylene (PP), three polyethylene (PE), four polyethylene terephthalate (PET), silicone, three cellulose/silicone mix, two paper/acrylate mix and one nylon samples. A composite FTIR spectrum is shown in **Figure 9A** and shows the major bands associated with PE,

TABLE 4 | Specific grinding energy.

Grinding specific energy	Integration time		
	1 τ_g	2 τ_g	3 τ_g
Torrefied un-densified material, kJ/kg (kWh/ton)	9.3 ± 0.8 (2.59)	25.7 ± 1.5 (7.13)	44.7 ± 2.5 (12.4)
PRB coal, kJ/kg (kWh/ton)	8.6 ± 0.5 (2.38)	24.3 ± 1.4 (6.75)	42.4 ± 2.4 (11.8)
Torrefied biomass, kJ/kg (kWh/ton)			43–54 (12–15)

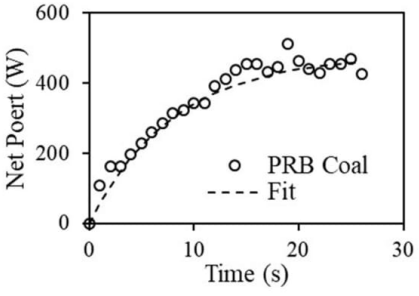

FIGURE 7 | Grinding power vs. time for PRB coal with τg = 9.1 (s).

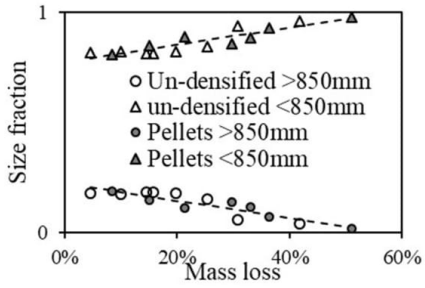

FIGURE 8 | Size fraction for the torrefied un-densified material and pellets vs. mass loss for size fractions under and above 850 μm.

TABLE 5 | Fraction <200 mesh of torrefied material in various mass losses.

Mass loss	Fraction <200 mesh
8.4%	67.0%
15.0%	73.9%
21.4%	77.3%
33.0%	77.5%
36.4%	89.2%
51.0%	95.4%

PP, PET and paper. No characteristic bands at 610 cm^{-1} (C-Cl stretch) and 1,425 cm^{-1} (C-H2 bending) were observed for polyvinylchloride (Krimm, 1963).

The major chemical changes that occurred upon torrefaction on densified and un-densified material and subsequent particle screening (<150 μm, 150<x<250 μm, 250<x<425 μm, 425<x<850 μm, and >850 μm) after grinding were also monitored by FTIR spectroscopy. The spectra for the ground screened 425<x<850 μm fraction for the densified torrefied (10, 20, and 42% mass loss) material as well as the CE-fiber mix are shown in **Figure 9A**. The spectra for the ground screened fractions for the un-densified torrefied (30% mass loss) material are shown in **Figure 9B**. Specific spectral bands can provide information on specific chemical changes that occur during thermal treatment (Balogun et al., 2017). All the samples had C-H stretching bands at assigned to methyl (2,960 and 2,870 cm^{-1}) and methylene (2,916 and 2,850 cm^{-1}) groups mainly associated with PP and PE plastic (Mayo, 2004a). In the ground screened torrefied material, plastic was generally concentrated in the larger sized fractions (425<x<850 μm and >850 μm) (**Figure 9B**). The O-H stretching band 3,100–3,600 cm^{-1} was present in all samples and progressively decreased in intensity upon the extent of torrefaction due to dehydration reactions (Wang et al., 2014; **Figure 9B**). A broad carbonyl (C=O) band at 1,690–1,750 cm^{-1} was observed and assigned to mainly an ester in linkage in PET and acrylate and an amide linkage in nylon (Mayo, 2004b). A small band at 1,505 cm^{-1} was assigned to lignin from paper (Faix, 1992). The spectral region between 1,000 and 1,070 cm^{-1} has been assigned to C–O stretching in wood cellulose and hemicellulose and decreased in intensity with torrefaction mass loss (Pandey, 1999). All samples were shown to have cis- and trans-vinylene bands at 727 and 974 cm^{-1}, respectively (Miller, 2004).

The relative changes in carbonyl, cellulose and hydroxyl content to methylene groups (plastic) that occurred during torrefaction were examined by calculating CI, CeI and HI, respectively (**Figure 10**). Low values of CI, CeI and HI means that there was a higher level of polyolefin plastic in the material. The CI generally decreased for all torrefied samples with an increase in particle size (from <150 μm to 425<x<850 μm), except for the >850 μm fraction (**Figure 10A**). For example, in the 30% mass loss torrefied material the CI decreased from 1.78 to 0.49 going from <150 μm to >850 μm particle size. For the low to moderate level of torrefaction (8–20% mass loss) the >850 μm fraction the higher CI values could be associated with higher levels of PET plastic. Furthermore, the CI levels were also shown

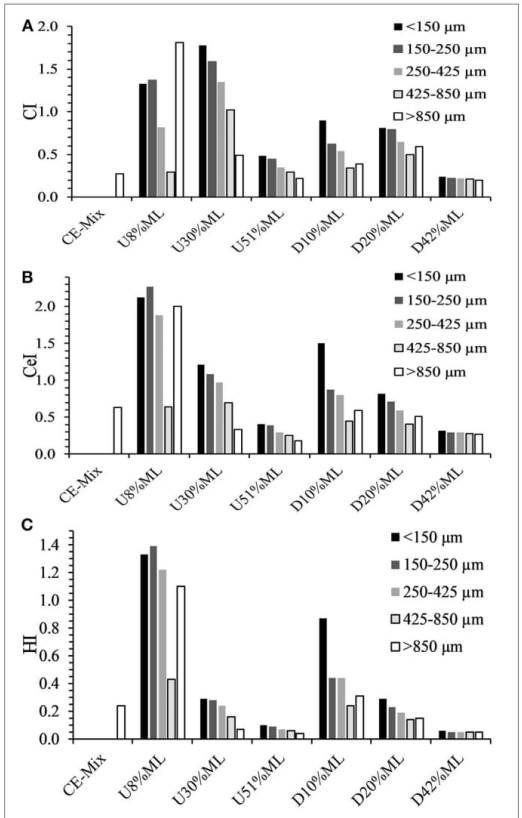

FIGURE 10 | Plots showing changes in **(A)** carbonyl index (CI), **(B)** cellulose index (CeI), and **(C)** hydroxyl index (HI) for ground screened fractions (<150 μm, 150<x<250 μm, 250<x<425 μm, 425<x<850 μm, and >850 μm) of torrefied densified (D) and un-densified (U) mate.

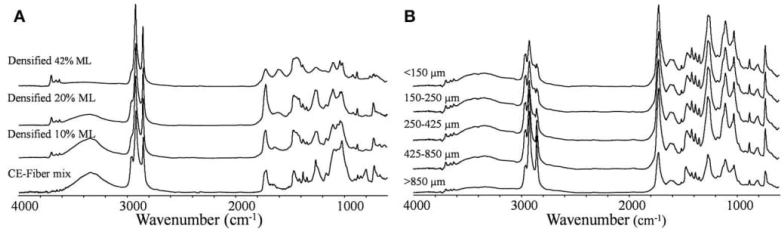

FIGURE 9 | FTIR spectra of **(A)** CE-fiber mix and ground/screened (425–850 μm) torrefied (10, 20, and 42% mass loss) densified material and **(B)** ground/screened (<150 μm, 150–250 μm, 250–425 μm, 425–850 μm, and >850 μm) un-densified torrefied (30% mass loss) material.

to decrease, associated with cleavage of the ester linkages in PET/acrylates and removal of the volatile degradation products (Çepeliogullar and Pütün, 2014), with the extent of torrefaction. Generally, for both CeI (**Figure 10B**) and HI (**Figure 10C**) decreased for all torrefied materials as screened particle size increased (<150 to >850 μm), suggesting that the cellulose fiber was mainly in the finer screened fractions. For example, in the 30% mass loss torrefied material the CeI and HI respectively decreased from 1.21 to 0.33 and 0.29 to 0.07 going from <150 to >850 μm particle size. Again, at low-moderate torrefaction levels (8–20% mass loss), the CeI and HI levels were high, suggesting that undegraded paper fragments were collected in the >850 μm fraction. Moreover, Both CeI and HI were shown to decrease as torrefaction severity increased. These findings support that the cellulose content decreased relative to plastic with the extent of torrefaction as a result of dehydration and degradation reactions (Wang et al., 2014).

Energy Content

The energy content was originally measured for un-sifted pulverized samples; however, it was discovered that scooping a sample of 1 g for the heat content test from a 200 g of the pulverized material gave very large scatter in the measured value. This was because the pulverized material has a large size distribution (as observed above) and the scooping did not necessarily give uniform size distribution. Therefore, it was decided to measure the heat content for five size fractions: x<150 μm, 150<x<250 μm, 250<x<425 μm, 425<x<850 μm, and x>850 μm separately. Although the heat content for all sifted samples in these size fractions, for the sake of brevity heat content was shown for the following consolidated fractions: x<150 μm, 150<x<850 μm, x>850 μm, and the calculated total heat content (from the fraction and heat content for each fraction). Heat content results presented here are dry- ash-free basis. **Figure 11** top-left is a plot of the heat content of the x<150 μm fraction as a function of mass loss. The point at zero mass loss is the heat content of the blend prior to torrefaction and the dashed line is a linear trend line to lead the eye. Clearly, the main source of this fraction was pulp fibers that increase heat content with an increase in mass loss as predicted by Klinger et al. (Klinger et al., 2013, 2015a,b). **Figure 11** top-right is a plot of the heat content of the 150 μm<x<850 μm fraction as a function of mass loss. The heat content does not seem to change with mass loss and has an average heat content of 35 ± 3 MJ/kg; this value was lower than that of plastic and it was assumed as a combination of fiber and plastic materials. **Figure 11** bottom-left is a plot of the heat content of the x>850 μm fraction as a function of mass loss. The heat content does not seem to change with mass loss and has an average heat content of 41.5 ± 3.0 MJ/kg; this value was similar to most of the plastic material (Sonawane et al., 2017) and thus was attributed as plastic. **Figure 11** bottom-right is a plot of the total heat content, as calculated from all fractions, as a function of mass loss. The slope of heat content increase was identical to that of the fiber.

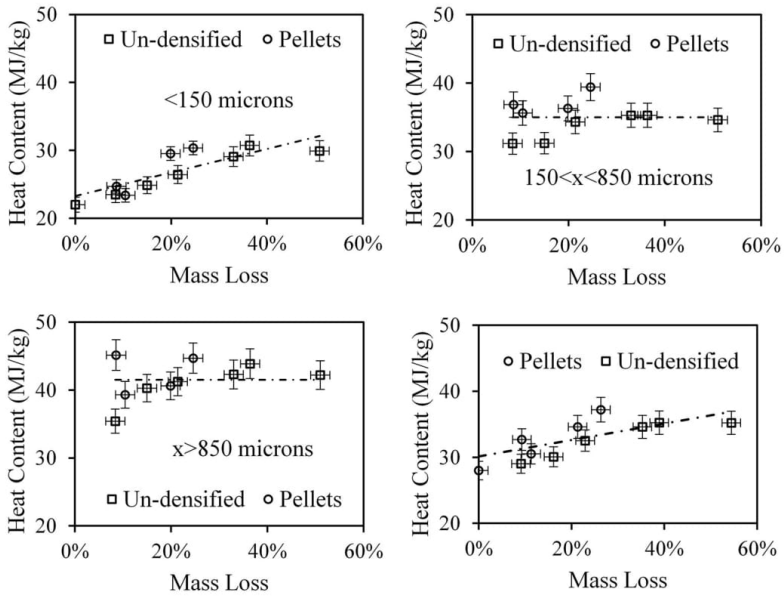

FIGURE 11 | Top left. Heat content of the size fraction x<150 μm. Top right, same for 150<x<850 μm. Bottom left. Same for x>850 μm. Bottom right. Total heat content.

Although the entire sample was pulverized, two materials (fibers and plastics) clearly retain their original structure which is indicated by the size distribution as shown above and the heat content as shown here. However, this material distinction diminishes as the torrefaction reaction proceeds (seen from the decrease of fraction x>850 μm). To further quantify this process, a plot of the contribution of the <850 μm fraction, which is a combination of torrefied material (from fibers) and fibers and the fraction >850 μm, which was entirely from plastic. **Figure 12** shows results of the contribution to the total energy from each fraction, showing that the contribution from plastics was about 20% at about 5–8% mass loss and became zero at 50% mass loss, where the plastic lost its original integrity.

Chlorine Removal

There was evidence that at the working temperatures of the torrefaction experiments (300°C) in this study, chlorine from the plastic materials should have been released as HCl (Saleh et al., 2014). Further, Bar-Ziv and Saveliev (2013) measured HCl in the torrefaction gas stream that was equivalent to the chlorine reduction in the solid phase. In the current study, numerous torrefaction experiments were performed as described above, and measured chlorine levels in the solid phase (see details above) with no evidence of any reduction of chlorine. This puzzling result can be explained by the way the current experiments were conducted, i.e., the sample was placed motionless. In this case, it was possible that in the time frame of the experiment, diffusion of HCl from the solid phase was so slow that it was not released during the experiment. However, in previous experiments by Bar-Ziv and Saveliev (2013), the material was torrefied in a stirred reactor (Zinchik et al., 2018) using much smaller size particles (∼1 mm) than in the present study and clearly showed that HCl was released.

As mentioned, high shear experiments with the torrefied material were conducted to obtain aqueous extracts which were filtered and measured for chloride in the solution and chlorine in the solid powder. **Figure 13** shows results of chlorine/chloride vs. mass loss; chlorine in solid after the high shear mixing and chloride in the filtrate (aqueous solution, adjusted for dilution). The scatter in the results was large and originate primarily from the fact that in these experiments, the samples were small (2–3 g) and the composition may differ significantly in its content and may not well represent the actual case. Nevertheless, there was a clear trend: (i) in the aqueous solution there was little-to-no chloride at zero mass loss (no torrefaction); (ii) the chloride in the aqueous solution increases gradually until ∼25% mass loss, after which it stays constant at an asymptotic value of 2,043 ± 207 ppm; (iii) chlorine in the solid phase has a value of 2,031 ± 129 at zero mass loss, then decreases gradually to ∼10% of the initial value.

SUMMARY AND CONCLUSION

In the present study blends of fiber and plastic wastes at a ratio of 60:40 (fiber-to-plastic) were used as feedstock for torrefaction. Both the un-densified material and pellets were torrefied at 300°C with different time periods. It was observed that the two forms have significantly different torrefaction dynamics. Un-densified material takes less time to start torrefaction compared to the pellets, which is due to the faster heat transfer to the un-densified material. The torrefied samples were characterized by moisture content, grindability, particle size distribution, energy content, molecular functional structure, and chlorine content. It was shown that although torrefaction dynamics is of the two forms differs significantly from each other, their properties depend on the mass loss. The fiber content was shown to decrease relative to plastic with the extent of torrefaction (mass loss) as determined by FTIR spectroscopy. Further, chemical (cellulose, hydroxyl, and carbonyl) changes were also shown to progressively decrease by torrefaction mass loss. Grinding characteristics, size distribution after grinding gave similar results as a function of mass loss during torrefaction, for the forms of material. Further, the torrefied product demonstrates

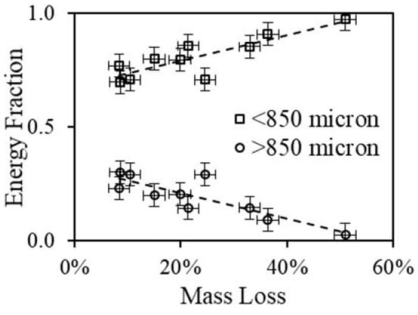

FIGURE 12 | Energy contribution of the above and under 850 μm size fractions to the total heat content of both un-densified material and pellets as a function of mass loss.

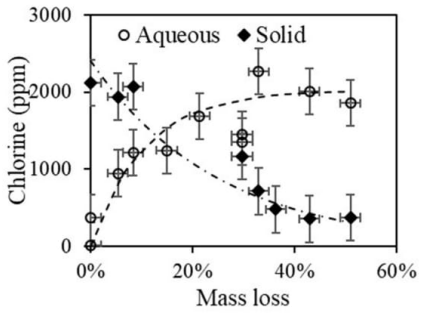

FIGURE 13 | Chlorine in solid filtrate after high shear mixing and chloride in the aqueous solution (adjusted for dilution).

a similar grinding behavior to PRB coal. The heat content of the material with size x>850 μm is much higher than that of size x<150 μm; the former attributed to the plastic material, whereas the latter was attributed to the fibers. The total heat content was shown to increase with mass loss. Chlorine in the torrefied samples was removed by a high shear mixing in aqueous solution showing that 5 min was sufficient to remove all chlorine after 30% mass loss. Overall, the waste blends studied in this paper showed that they can be used as drop-in fuel in coal power generation facilities, since this fuel is sustainable and low-cost, it also meets the environ mental regulation standard.

AUTHOR CONTRIBUTIONS

ZX carried out torrefaction experiments and characterization for heat and moisture content, grinding and size fractions. SZ helped in all above plus carried out some of the modeling work and took part in data analysis. SK carried our chloride extraction and characterization. AM analyzed the samples by FTIR spectroscopy and contributed to the manuscript in the appropriate sections and editing. TH and DC prepared the materials, characterized them and determined chlorine content in the solid phase. EB-Z supervised the entire work, analyzed the data, carried out the modeling work and wrote most of the paper.

REFERENCES

Balogun, A., Sotoudehniakarani, F., and McDonald, A. G. (2017). Thermo-kinetic, spectroscopic study of brewer's spent grains and characterization of their pyrolysis products. *J. Anal. Appl. Pyrol.* 127, 8–16. doi: 10.1016/j.jaap.2017.09.009.

Bar-Ziv, E., Klinger, J., Zinchik, S., and Donepudi, Y. (2016). *Torrefied-Biomass from Municipal Solid Waste For Power Production*. ASME-PowerEnergy 2016–59179.

Bar-Ziv, E., and Saveliev, R. (2013). *Torrefied-Biomass from Municipal Solid Waste for Power Production*. ASME-Power 2013-98044.

Bates, R. B., and Ghoniem, A. F. (2013). Biomass torrefaction: modeling of reaction thermochemistry. *Biores. Technol.* 134, 331–340. doi: 10.1016/j.biortech.2013.01.158

Çepeliogullar, O., and Pütün, A. E. (2014). A pyrolysis study for the thermal and kinetic characteristics of an agricultural waste with two different plastic wastes. *Waste Manage. Res.* 32, 971–979. doi: 10.1177/0734242X14542684

Demirbas, A. (1999). Physical properties of briquettes from waste paper and wheat straw mixtures. *Energy Conver. Manage.* 40, 437–445. doi: 10.1016/S0196-8904(98)00111-3

De Rezende Pinho, A., De Almeida, M. B., Mendes, F. L., Casavechia, L. C., Talmadge, M. S., Kinchin, C. M., et al. (2017). Fast pyrolysis oil from pinewood chips co-processing with vacuum gas oil in an FCC unit for second generation fuel production. *Fuel* 188, 462–473. doi: 10.1016/j.fuel.2016.10.032

Donepudi, Y. (2017). *Impact of Pretreatment Methods on Fast Pyrolysis of Biomass*. Houghton, MI: Michigan Technological University.

EPA (Environmental Protection Agency) (2015). *Carbon Pollution Emission Guidelines for Existing Stationary Sources: Electric Utility Generation Units*. EPA-HQ-OAR-2013-0602, 1560.

EPA (Environmental Protection Agency) (2014). *Carbon Pollution Emission Guidelines for Existing Stationary Sources: Electric Utility Generating Units*. Federal Register. Environmental Protection Agency.

EPA (Environmental Protection Agency) (2016). *Assessing Trends in Material Generation, Recycling, Composting, Combustion with Energy Recovery and Landfilling in the United States*. Report EPA530-R-17-01, 91 pp., Nov. 2016.

Faix, O. (1992). "Fourier transform infrared spectroscopy," in *Methods in Lignin Chemistry*, eds S. Y. Lin and C. W. Dence (Berlin: Springer-Verlag), 83–132.

Funke, A., Henrich, E., Dahmen, N., and Sauer, J. (2017). Dimensional analysis of auger-type fast pyrolysis reactors. *Energy Technol.* 5, 119–129. doi: 10.1002/ente.201600095

Helble, J. J., Srinivasachar, S., and Boni, A. A. (1990). Factors influencing the transformation of minerals during pulverized coal combustion. *Prog. Energy Combustion Sci.* 16, 267–279. doi: 10.1016/0360-1285(90)90036-3

Incropera, F. P., and DeWitt, D. P. (2002). *Fundamentals of Heat and Mass Transfer*. New York, NY: J. Wiley.

Iroba, K. L., Baik, O. D., and Tabil, L. G. (2017a). Torrefaction of biomass from municipal solid waste fractions I: temperature profiles, moisture content, energy consumption, mass yield, and thermochemical properties. *Biomass Bioenergy* 105, 320–330. doi: 10.1016/j.biombioe.2017.07.009

Iroba, K. L., Baik, O. D., and Tabil, L. G. (2017b). Torrefaction of biomass from municipal solid waste fractions II: grindability characteristics, higher heating value, pelletability and moisture adsorption. *Biomass Bioenergy* 106, 8–20. doi: 10.1016/j.biombioe.2017.08.008

Khalsa, J., Leistner, D., Weller, N., Darvell, L. I., and Dooley, B. (2016). Torrefied biomass pellets - comparing grindability in different laboratory mills. *Energies* 9, 1–16. doi: 10.3390/en9100794

Kiel, J. (2011). "Torrefaction for upgrading biomass into commodity fuel," in *Status and ECN Technology Development. EUBIONET III Workshop* (Espoo).

Klinger, J., Bar-Ziv, E., and Shonnard, D. (2013). Kinetic study of aspen during torrefaction. *J. Anal. Appl. Pyrol.* 104, 146–152. doi: 10.1016/j.jaap.2013.08.010

Klinger, J., Bar-Ziv, E., and Shonnard, D. (2015a). Unified kinetic model for torrefaction-pyrolysis. *Fuel Process. Technol.* 138, 175–183. doi: 10.1016/j.fuproc.2015.05.010

Klinger, J., Bar-Ziv, E., Shonnard, D., Westover, T., and Emerson, R. (2015b). Predicting properties of gas and solid streams by intrinsic kinetics of fast pyrolysis of wood. *Energy Fuels* 30, 318–325. doi: 10.1021/acs.energyfuels.5b01877

Krimm, S. (1963). Infrared spectra and assignments for polyvinyl chloride and deuterated analogs. *J. Polymer Sci. Part A* 1, 2621–1650. doi: 10.1002/pol.1963.100010809

Kumar, L., Koukoulas, A. A., Mani, S., and Satyavolu, J. (2017). Integrating torrefaction in the wood pellet industry: a critical review. *Energy Fuels* 31, 37–54. doi: 10.1021/acs.energyfuels.6b02803

Lédé, J. (2010). Biomass pyrolysis: comments on some sources of confusions in the definitions of temperatures and heating rates. *Energies* 3, 886–898. doi: 10.3390/en3040886

Luppens, J. A. (2011). *A Critical Review of Published Coal Quality Data from the Southwestern Part of the Powder River Basin*. Geological Survey Open-File Report, Wyoming, 2011-1148, 23.

Mason, P. E., Darvell, L. I., Jones, J. M., and Williams, A. (2016). Comparative study of the thermal conductivity of solid biomass fuels. *Energy Fuels* 30, 2158–2163. doi: 10.1021/acs.energyfuels.5b02261

Mayo, D. W. (2004a). "Characteristics of alkanes," in *Course Notes on the Interpretation of Infrared and Raman Spectra*, eds D. W. Mayo, F. A. Miller, and R. W. Hannah (New Jersey, NY: John Wiley & Sons), 33–72.

Mayo, D. W. (2004b). "Spectra of carbonyl compounds of all kinds (Factors affecting carbonyl group frequencies," in *Course Notes on the Interpretation of Infrared and Raman Spectra*, eds D. W. Mayo, F. A. Miller, and R. W. Hannah (New Jersey, NY: John Wiley & Sons), 79–204.

McCabe, J. G. (2014). *Addressing Biogenic Carbon Dioxide Emissions from Stationary Sources*. Washington, DC: United States Environmental Protection Agency.

McKendry, P. (2002). Energy production from biomass (part 2): conversion technologies. *Biores. Technol.* 83, 47–54. doi: 10.1016/S0960-8524(01)00119-5

Miller, F. A. (2004). "Characteristic frequencies of alkenes (olefins)," in *Course Notes on the Interpretation of Infrared and Raman Spectra*, eds D. W. Mayo, F. A. Miller, and R. W. Hannah (New Jersey, NY: John Wiley & Sons), 73–84.

Miranda, R., Sosa-Blanco, C., Bustos-Martínez, D., and Vasile, C. (2007). Pyrolysis of textile waste I. kinetics and yields. *J. Anal. Appl. Pyrol.* 80, 489–495. doi: 10.1016/j.jaap.2007.03.008

Mu'min, G. G., Prawisudha, P., Zaini, I. N., Aziz, M., and Pasek, A. D. (2017). Municipal solid waste processing and separation employing wet torrefaction

for alternative fuel production and aluminum reclamation. *Waste Manage.* 67, 106–120. doi: 10.1016/j.wasman.2017.05.022

Nakamura, D., and Mufson, S. (2014). China, U.S. Agree to Limit Greenhouse Gases. *The Washington Post,* p. 12.

Pandey, K. K. (1999). A study of chemical structure of soft and hardwood and wood polymers by FTIR spectroscopy. *J. Appl. Polym. Sci.* 71, 1969–1975. doi: 10.1002/(SICI)1097-4628(19990321)71:12<1969::AID-APP6>3.0.CO;2-D

Patterson, J. E., and Miers, R. J. (2010). "The thermal conductivity of common tubing materials applied in a solar water heater collector," in *46th ASC Annual International Conference, Wentworth Institute of Technology*, ed T. Sulbaran (Boston, MA).

Radics, R. I., Gonzales, R., Bilek, E. M., and Kelley, S. S. (2017). Systematic review of torrefied wood economics. *BioResources* 12, 6868–6886. doi: 10.15376/biores.12.3.Radics

Saleh, S. B., Flensborg, J. P., Shoulaifar, T. K., Sárossy, Z., Hansen, B. B., Egsgaard, H., et al. (2014). Release of chlorine and sulfur during biomass torrefaction and pyrolysis. *Energy Fuels* 28, 3738–3746. doi: 10.1021/ef4021262

Sonawane, Y. B., Shindikar, M. R., and Khaladkar, M. Y. (2017). High calorific value fuel from household plastic waste by catalytic pyrolysis. *Nat. Environ. Pollut. Technol.* 16, 879–882.

Storm, R. F. (2009). " Blueprint" your pulverizer for improved performance. *Power* 153, 60–63.

Themelis, N. J., and Mussche, C. (2014). *Energy and Economic Value of Municipal Solid Waste (MSW), Including Non-Recycled Plastics (NRP), Currently Landfilled in the Fifty States*. New York, NY: Earth Engineering Center, Columbia University.

TRI, ThermoChem Recovery International (2018). *"Reforming gasification," 2017*. Available online at: http://tri-inc.net/steam-reforming-gasification/

Unapumnuk, K., Keener, T. C., Lu, M., and Khang, S. J. (2006). Pyrolysis behavior of tire-derived fuels at different temperatures and heating rates. *J. Air Waste Manage. Assoc.* 56, 618–627. doi: 10.1080/10473289.2006.10464481

US-EIA (2018). *U.S. Energy Information Administration, "Monthly Energy Review"*. DOE/EIA0035.

US-EIA (2010). *U.S. Energy Information Administration, Based on U.S. Environmental Protection Agency, 2010 MSW Facts and Figures Factsheet*. Associates. Available online at: https://www.eia.gov/todayinenergy/detail.php?id=8010 (Accessed Nov 11, 2018).

Wang, C., Li, M., and Fang, Y. (2016). Coprocessing of catalytic-pyrolysis-derived bio-oil with vgo in a pilot-scale FCC Riser. *Ind. Eng. Chem. Res.* 55, 3525–3534. doi: 10.1021/acs.iecr.5b03008

Wang, L., Barta-Rajnai, E., Skreiberg, Ø., Khalil, R. A., Czégény, Z., Jakab, E., et al. (2017). Impact of torrefaction on woody biomass properties. *Energy Procedia* 105, 1149–1154. doi: 10.1016/j.egypro.2017.03.486

Wang, Z., Pecha, B., Westerhof, R., Kersten, S., Li, C.-Z., McDonald, A. G., et al. (2014). Effect of cellulose crystallinity on solid/liquid phase reactions responsible for the formation of carbonaceous residues during slow pyrolysis. *Ind. Eng. Chem. Res.* 53, 2940–2955. doi: 10.1021/ie4014259

Wei, L., McDonald, A. G., Freitag, C., and Morrell, J. J. (2013). Effects of wood fiber esterification on properties, weatherability and biodurability of wood plastic composites. *Polymer Degrad. Stability* 98, 1348–1361. doi: 10.1016/j.polymdegradstab.2013.03.027

White, E. D. (2014). The supreme court of the U.S. *Am. Bar Assoc. J.* 7, 341–343.

Yuan, H., Wang, Y., Kobayashi, N., Zhao, D., and Xing, S. (2015). Study of fuel properties of torrefied municipal solid waste. *Energy Fuels* 29, 4976–4980. doi: 10.1021/ef502277u

Zhao, W., Liu, D., and Zhang, Y. (2017). Study on the influence of pressure-assisted thermal processing on PET/PE via the change of melting enthalpy. *J. Food Process. Preserv.* 41:e13135. doi: 10.1111/jfpp.13135

Zhu, Q. (2014). *Coal Sampling and Analysis Standards*. London: IEA Clean Coal Centre.

Zinchik, S., J. L., Klinger, T. L., Westover, Y., Donepudi, S., and Hernandez, J. D., Naber, et al. (2018). Evaluation of fast pyrolysis feedstock conversion with a mixing paddle reactor. *Fuel Process. Technol.* 171, 124–132. doi: 10.1016/j.fuproc.2017.11.012

Conflict of Interest Statement: The authors declare that the research was conducted in the absence of any commercial or financial relationships that could be construed as a potential conflict of interest.